Eur. Phys. J. A (2013) **49**: 138
DOI 10.1140/epja/i2013-13138-0

THE EUROPEAN PHYSICAL JOURNAL A

Regular Article – Experimental Physics

Design studies of the PWO Forward End-cap calorimeter for $\overline{\text{P}}$ANDA

for the $\overline{\text{P}}$ANDA Collaboration*

H. Moeini[1,a], M. Al-Turany[2], M. Babai[1], A. Biegun[1], O. Bondarenko[1], K. Götzen[2], M. Kavatsyuk[1], M.F. Lindemulder[1], H. Löhner[1], D. Melnychuk[3], J.G. Messchendorp[1], H.A.J. Smit[1], S. Spataro[4], and R. Veenstra[1]

[1] Kernfysisch Versneller Instituut (KVI), University of Groningen, Groningen, The Netherlands
[2] GSI Helmholtzzentrum für Schwerionenforschung GmbH, Germany
[3] National Centre for Nuclear Research, Warsaw, Poland
[4] Dipartimento di Fisica, Università di Torino and INFN, Italy

Received: 6 June 2013 / Revised: 16 September 2013
Published online: 6 November 2013

Communicated by M. Guidal

Abstract. The $\overline{\text{P}}$ANDA detection system at FAIR, Germany, is designed to study antiproton-proton annihilations, in order to investigate, among others, the realm of charm-meson states and glueballs, which has still much to reveal. The yet unknown properties of this field are to be unraveled through studying QCD phenomena in the non-perturbative regime. The multipurpose $\overline{\text{P}}$ANDA detector will be capable of tracking, calorimetry, and particle identification, and is planned to run at high luminosities providing average reaction rates up to $2 \cdot 10^7$ interactions/s. The envisaged physics program requires measurements of photons and charged particles with excellent energy, position, and time resolutions. The electromagnetic calorimeter (EMC) will serve as one of the basic components of the detector setup and comprises cooled lead-tungstate ($PbWO_4$) crystals. This paper presents the mechanical design of the Forward End-cap calorimeter and analyzes the response of the Forward End-cap calorimeter in conjunction with the full EMC and the complete $\overline{\text{P}}$ANDA detector. The simulation studies are focused on the performance of the planned EMC with respect to the energy and spatial resolution of the reconstructed photons. Results of the Monte Carlo simulations, excluding very low-energy photons, have been validated by data obtained from a prototype calorimeter and shown to fulfil the requirements imposed by the $\overline{\text{P}}$ANDA physics program.

1 Introduction

The $\overline{\text{P}}$ANDA Experiment [1] will be one of the key experiments in hadron physics at the Facility for Antiproton and Ion Research (FAIR) at Darmstadt, Germany. The central part of FAIR is a synchrotron complex providing intense pulsed ion beams ranging from protons to uranium. Antiprotons with a momentum between 1.5 GeV/c and 15 GeV/c, produced by a primary proton beam, will be stored and cooled in the High Energy Storage Ring (HESR) and interact in a fixed target geometry in the $\overline{\text{P}}$ANDA detector. In the high resolution mode, a RMS momentum resolution $\frac{\sigma_p}{p} \leq 4 \cdot 10^{-5}$ is envisaged for the beam momenta between 1.5 GeV/c and 8.9 GeV/c. The average peak luminosity of $2 \cdot 10^{31}\,\text{cm}^{-2} \cdot \text{s}^{-1}$ for 10^{10} $\overline{\text{p}}$ is expected for this mode, assuming $\rho_{target} = 4 \cdot 10^{15}\,\text{atoms} \cdot \text{cm}^{-2}$. With the same target density and for 10^{11} $\overline{\text{p}}$, an average peak luminosity of $2 \cdot 10^{32}\,\text{cm}^{-2} \cdot \text{s}^{-1}$ is expected for the high-luminosity mode, providing a RMS momentum spread of $\frac{\sigma_p}{p} \approx 10^{-4}$ over the momentum range of 1.5 GeV/c to 15 GeV/c [2]. A hydrogen cluster jet or a hydrogen pellet target will allow an average interaction rate of up to 20 MHz. Contrary to e^+e^- collisions, states of all non-exotic quantum numbers can be formed directly in antiproton-proton annihilations. This allows mass and width measurements of hadronic resonances by the beam-scanning technique [1,3] with an accuracy of 50–100 keV, which is 10 to 100 times better than realized in any e^+e^- collider experiment.

In order to collect all the relevant kinematic information from the final states of the antiproton-proton collisions, the experiment employs the versatile $\overline{\text{P}}$ANDA detector which is able to provide precise trajectory reconstruction, measure energy and momentum of particles with high resolution, and efficiently identify the charged particles. The detector (fig. 1) is subdivided into two magnetic spectrometers: the Target Spectrometer (TS),

* http://www-panda.gsi.de
[a] e-mail: moeini@kvi.nl

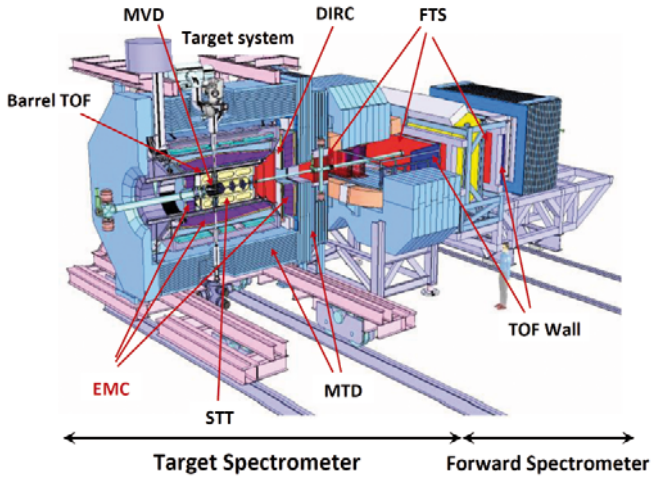

Fig. 1. Schematic view of the $\overline{\text{P}}$ANDA detector consisting of Target Spectrometer (located inside the solenoid magnet) and Forward Spectrometer. The EMC, as part of the target spectrometer, and other detector elements are labeled in the figure with explanations given in the text. The scale is indicated by the person in the figure.

located inside a 2 T superconducting solenoid magnet surrounding the interaction point and covering angles from 5° (10°) to 170° in the vertical (horizontal) plane; the Forward Spectrometer (FS), based on a dipole magnet with a field integral of up to 2 Tm to momentum analyze forward-scattered particles in the region of angles up to 5° (10°). The combination of the two spectrometers allows for tracking, momentum reconstruction, charged-particle identification, and electromagnetic calorimetry as well as muon identification in a close to 4π geometry. The various elements of the $\overline{\text{P}}$ANDA detector system include the Micro Vertex detector (MVD), Straw Tube Tracker (STT), Gas Electron Multiplier (GEM), Cherenkov detectors (DIRC: Detection of Internally Reflected Cherenkov light), Forward Tracking Stations (FTS), Muon Tracking Detector (MTD), Aerogel Ring Imaging Cherenkov Counter (RICH), Time Of Flight System (SciTil), the Electromagnetic Calorimeter (EMC), and the Forward Time-Of-Flight Wall (FTOF).

The experiment focuses on hadron spectroscopy, in particular on the search for exotic states in the charmonium mass region, on the interaction of charmed hadrons with the nuclear medium, on double-hypernuclei to investigate the nuclear potential and hyperon-hyperon interactions as well as on electromagnetic processes to study various aspects of nucleon structure [3]. These physics objectives define the requirements for the $\overline{\text{P}}$ANDA detector system in which the EMC plays a crucial role. For precision spectroscopy of charmonium states and exotic hadrons in the charmonium region a full acceptance is required to allow for a proper partial-wave analysis. Accordingly, as final states with many photons can occur, a low photon threshold of about 10 MeV is a key requirement for the electromagnetic calorimeter. Consequently, a 2–3 MeV threshold for individual crystals and low noise levels of about 1 MeV are required.

This paper demonstrates the performance of one of the important modules of the EMC, the Forward End-cap calorimeter in conjunction with other EMC modules[1]. To this end the mechanical design, as implemented in the Monte Carlo simulation tool, will be explained in sect. 2. The analysis that is presented throughout the paper will not be applicable for very low-energy photons. The results of the Monte Carlo simulations, based on experimental studies of the prototype, will be discussed in sect. 3, and the performance of the detection system for the benchmark physics channel $\overline{p} + p \to h_c \to \eta_c + \gamma \to (\pi^0 + \pi^0 + \eta) + \gamma \to 7\gamma$ will be presented in sect. 4. Although all the EMC modules (including Forward End-cap, Backward End-cap, and Barrel) will be employed for the complete reconstruction of this decay channel, the optimized parameters for the energy reconstruction that are obtained from a prototype setup made of Barrel-type crystals will be exploited for the Barrel crystals. Such an energy optimization is required for Barrel crystals due to light yield non-uniformities (see sect. 3.3.3) which appear to be absent in the End-cap crystals. Simulation results, excluding very low-energy photons, will show that the proposed technical design of the calorimeter meets the requirements imposed by the $\overline{\text{P}}$ANDA physics program.

2 The electromagnetic calorimeter of $\overline{\text{P}}$ANDA

2.1 Operating conditions and layout

In the TS, high-precision electromagnetic calorimetry is required over a large energy range from a few MeV up to 15 GeV. Lead-tungstate ($PbWO_4$ or briefly PWO) is chosen as calorimeter material in the TS due to its fast response and correspondingly high count-rate capability, and its high density which allows for a compact setup. Despite the low light yield, PWO revealed good energy resolution for photon and electron detection at intermediate energies [4], which motivates the detailed response study presented here. The high granularity and maximum acceptance of the EMC are needed, in order to discriminate pions from electrons for momenta above 0.5 GeV/c. In high-energy physics PWO has been chosen by the CMS Collaboration at CERN [5]. For $\overline{\text{P}}$ANDA, it is proposed to use crystals with a length of 200 mm ($\approx$ 22 radiation lengths), which allows optimum shower containment for photons up to 15 GeV and limits the nuclear counter effect in the subsequent photo-sensor to a tolerable level, in order to achieve an energy resolution (σ/E) for photons and electrons of $1.95(4)\%/\sqrt{E[\text{GeV}]} + 0.48(5)\%$ [6]. All crystals will be cooled down to −25 °C to provide a light yield of 500 photons/MeV which constitutes an overall gain factor of 3.5 as compared to the operation at +18 °C.

[1] The intention of this paper is to study constraints imposed by the mechanical design rather than giving a description of the complete technical design and analysis of the Forward End-cap.

Since $\overline{\mathrm{P}}$ANDA is a fixed-target experiment, produced particles are boosted in the forward direction and the event-rate distribution in the EMC is not isotropic. An average event rate of 10 to 100 kHz is expected in the central part around the interaction region covered by the Barrel EMC, whereas the forward region covered by the Forward End-cap EMC (FwEndCap) will be exposed to event rates of up to 500 kHz. Thus, two large-area avalanche photodiodes (LAAPD) [3], each having a 100 mm^2 area, will be used as photo-sensors for the Backward End-cap EMC (BwEndCap), the Barrel, and the outermost 80% crystals of the FwEndCap. The innermost 20% crystals of the FwEndCap will be equipped with vacuum photo-tetrodes (VPTT) [3], in order to adapt to the expected extreme high rates of up to 500 kHz in the region nearest to the beam axis.

The $\overline{\mathrm{P}}$ANDA PWO crystals will be arranged in the cylindrical Barrel with a length of 2.5 m and an inner radius of about 57 cm (11360 crystals), in the BwEndCap (528 crystals), and in the FwEndCap (3856 crystals). These three separate parts of the EMC, referred to as EMC modules in the target spectrometer, will be placed inside the 2 T solenoid magnet of the TS. The basic crystal shapes are squared-profile prismoids with two of their neighboring sides being right-angled trapezoids, based on the "flat-pack" configuration used in the CMS calorimeter [7]. The dimensions of the crystals are about $20 \times 20 \times 200\,\mathrm{mm}^3$ for the Barrel and BwEndCap. The same crystal length of 200 mm is used for the FwEndCap, but with slightly larger crystal areas of $24.37 \times 24.37\,\mathrm{mm}^2$ at the front and $26 \times 26\,\mathrm{mm}^2$ at the rear faces.

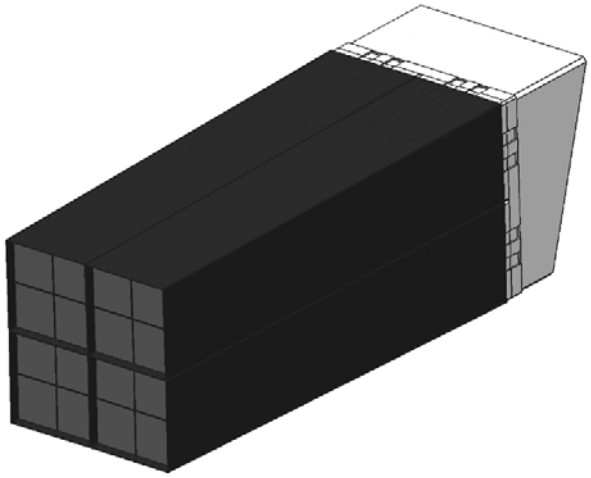

Fig. 2. Subunit of 16 crystals assembled in a carbon-fiber alveole with mounting interface.

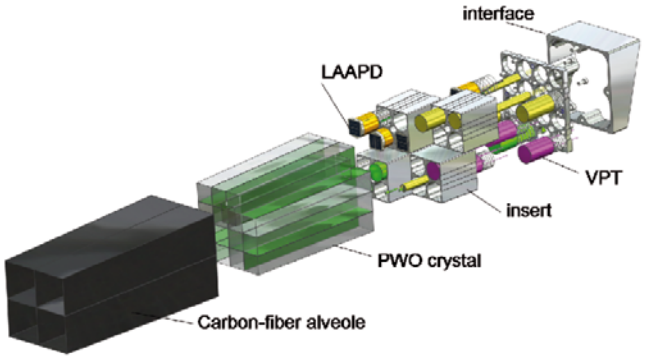

Fig. 3. Exploded view of one subunit with (looking from the left): carbon-fiber alveole separating the boxes in a subunit, 16 crystals of a subunit, inserts holding either LAAPD or VPTT photo-sensors, and the mounting interface. Only one sort of photo-sensor is used in a subunit.

2.2 The FwEndCap verification strategy

The preliminary concepts related to the EMC detector are detailed in the Technical Design Report [3]. The FwEndCap design has to fulfil the demands imposed by the physics program of $\overline{\mathrm{P}}$ANDA. This requires measurements of photons and charged particles with a good energy, time, and spatial resolution. It is extremely important that the FwEndCap can take the high count rates with a sufficient resolution without being damaged. The complete coverage of the forward region is necessary for the most efficient reconstruction of all reaction products.

Inspired by the CMS design [5], the mechanical layout of the FwEndCap was designed according to the requirements and geometrical restrictions of the $\overline{\mathrm{P}}$ANDA detector. In connection with the development of the computing framework PandaROOT [8] for $\overline{\mathrm{P}}$ANDA, the verification of the mechanical design through simulations and a validation with experimental results is mandatory. PandaROOT is a framework for both simulations and data analysis, and is mainly based on the object-oriented data analysis framework ROOT [9]. It features the concept of Virtual Monte Carlo [10], which allows to run transport models `Geant3` and `Geant4` [11] using the same code, making it easy to compare the results of various transport models with exactly the same conditions. Using PandaROOT the designed geometry of the FwEndCap (crystals and carbon-fiber packages) was used for detector simulation. The simulation results will be discussed in the remainder of this article. Here, all the simulation results are obtained using the `Geant3` transport model and a production cut energy of 1 MeV is imposed for secondary particles.

2.3 The FwEndCap technical design

Based on the technical design of the FwEndCap, 16 crystals will be composed in packages called subunits (see fig. 2). A schematic representation of the various components forming a subunit is shown in fig. 3. The crystals of a subunit are contained by a layer of 0.18 mm carbon-fiber material (see fig. 4) forming the walls of a container called *alveole* which was produced by Fiberworx BV [12] according to our design specifications. Two side-by-side boxes in the geometry of the FwEndCap are separated by a 0.36 mm thick alveole wall.

In the simulations, every four crystals are arranged in a box of 2×2 crystals, which is a squared-profile right

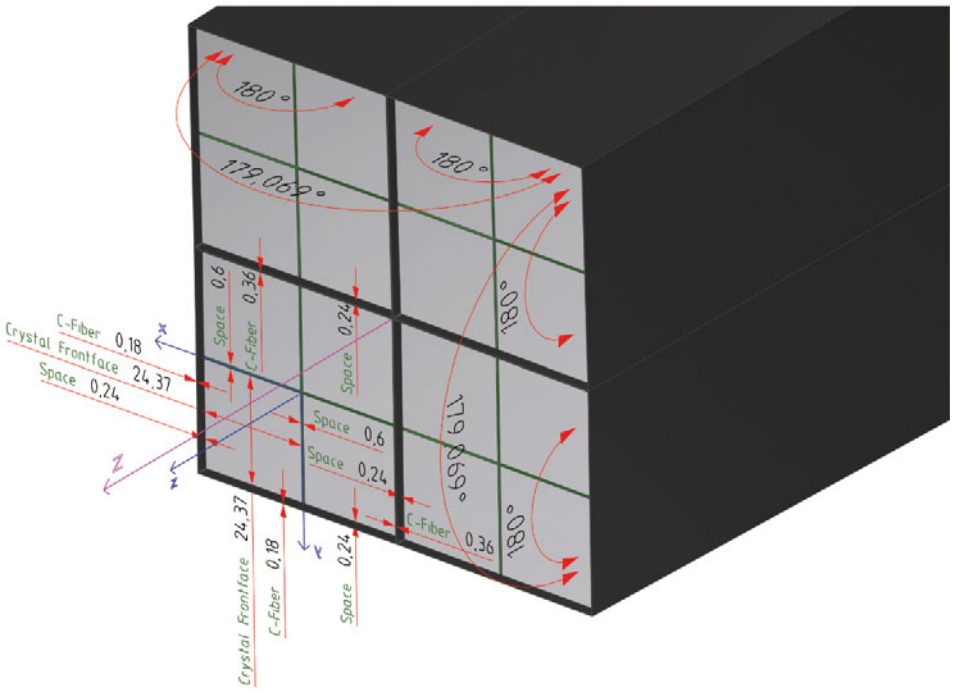

Fig. 4. Dimensions of the subunit construction (in mm). Groups of four crystals are arranged in a box with a planar front face. The front faces of either two boxes are slightly tilted with a relative angle of ca. 1°. The central axes of a box (z) and of the subunit (Z) are indicated. The width of a crystal and the thickness of the carbon-fiber walls and gaps are shown.

prismoid or, technically, a frustum (truncated pyramid). The specific shape of the crystals ensures that all the front and rear faces of the crystals in a box lie on two parallel planes 200 mm apart. Every subunit comprises four identical boxes whose symmetry axes are slightly rotated with respect to the subunit symmetry axis (Z in fig. 4). The boxes are rotated around the axes x and y of a box by the same angle ($\Delta\theta_y = \Delta\theta_x = \mathrm{atan}[24.37/3000]$) in such a way that each box would face straight toward the so-called *off-point* of the subunit. This is a point on the symmetry axis of the subunit at which the symmetry axes of the four boxes intersect, and that is about 3088 mm away from the front face of the subunit. This value is exactly the same in both the mechanical and the simulation design, and can be deduced from the distances and angles given in fig. 4, since $[24.37 + (0.36/2) + 0.24 + (0.6/2)]\,\mathrm{mm}/\tan[(180° - 179.069°)/2] = 3088\,\mathrm{mm}$. The considered spaces between the crystals in a box and between the box and the alveole walls are reserved for the wrapping material of about 0.07 mm thickness as well as a tolerance space to be filled with air.

For the ease of construction, the mechanical design of the FwEndCap with a nearly circular periphery was constrained to contain only full- or half-subunit packages of crystals. It will contain 214 complete subunits and 54 half-subunits in total, which sums up to the total number of 964 (3856) boxes (crystals) in the FwEndCap. Figure 4 quantifies various gaps between the crystals and thicknesses of alveole walls in different parts of a subunit. Figure 5 shows a view of the complete mechanical design of the FwEndCap with thermal insulation cover and other details. Although the FwEndCap is built with tapered

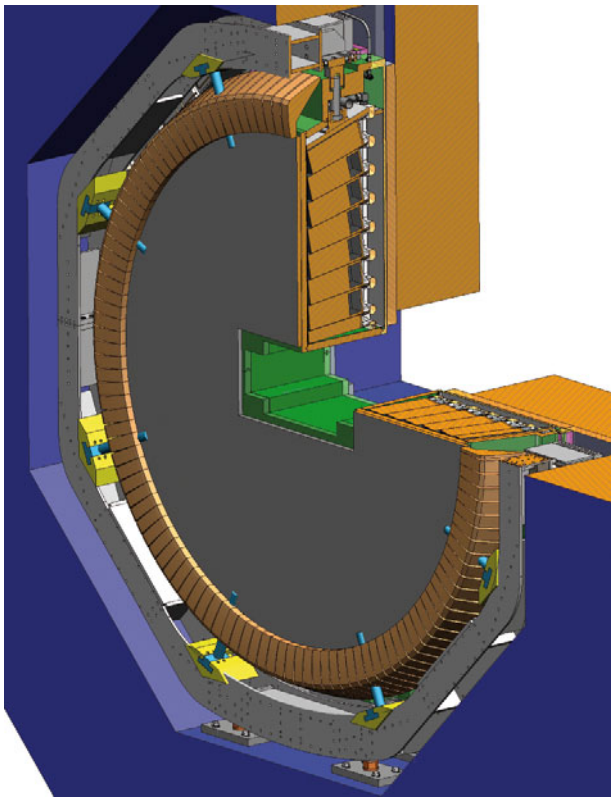

Fig. 5. A view of the complete mechanical design of the FwEndCap with thermal insulation cover and holding structure. The Disc DIRC Cherenkov detector is placed in front of the crystals in the same frame which is inserted in the solenoid magnet of the target spectrometer.

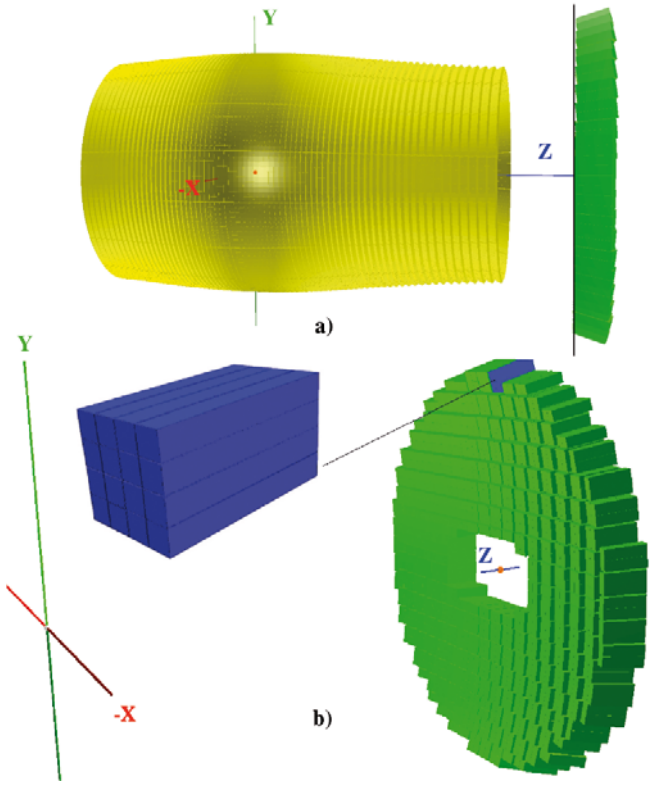

Fig. 6. (a) A side view of the Barrel and FwEndCap of the $\overline{\text{P}}$ANDA EMC based on the PandaROOT simulation package. The position of the front plane is shown as a black vertical line. (b) Geometrical layout of the nearly planar arrangement of the FwEndCap; each block represents a half- or full-subunit; one subunit is shown in an expanded view. This comprises crystals numbered as row = 34–37 and column = 3–6 in the simulation code.

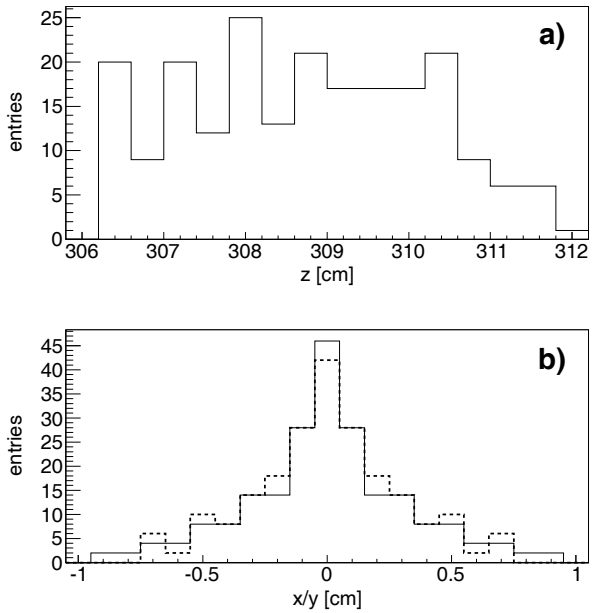

Fig. 7. The distribution of the points of closest approach of the symmetry axes of all full-subunits of the FwEndCap to the beam axis; (a) The distance distribution of the points of closest approach in beam direction with respect to the front plane of the FwEndCap (off-point value). The mean value of this distribution is 3088 mm, as designed; (b) The distribution of the points of closest approach in the x- (solid line) and y-direction (dashed line).

crystals, the subunits are arranged in a quasi-planar geometry perpendicular to the beam axis, in order to ensure a compact setup inside the solenoid. Consequently, the subunits at larger angles are pulled downstream such that the front tip of at least one crystal stays on one plane and the front tips of all other crystals stay behind this plane, defined as the *front plane* (see fig. 6). Every full- or half-subunit is to be fixed onto a 30 mm thick aluminium backplane by pre-angled interface pieces (see fig. 3) to keep the exact position and orientation. The optimized orientation of the aluminium interfaces and, correspondingly, subunits and half-subunits are calculated with UGS NX 5 [13]. These mechanical-design values have been taken to implement the geometry of the FwEndCap into the simulation code.

2.4 The FwEndCap implementation in PandaROOT

Figure 6 shows the Barrel and FwEndCap of the EMC as drawn within the PandaROOT framework. The maximum polar angle coverage of the FwEndCap is calculated to be 24°. This would contain 72 columns and 74 rows of crystals of the FwEndCap. Within the simulations, the crystal column and row numbers range, respectively, from −36 to 36 and −37 to 37, excluding 0. Figure 7 shows the distribution of the points of closest approach of the symmetry axes of the subunits to the beam axis. The distance distribution of the points of closest approach with respect to the front plane of the FwEndCap is shown in fig. 7 a). We call this distance the *off-point value* of the subunit, which is slightly different for various subunits because of the planar construction. In principle, we expect 57 different off-point values due to the symmetry of the FwEndCap design. The target point has a distance of 2039 mm to the front plane of the FwEndCap, while the mean value of the off-point-value histogram indicates a distance of about 3088 mm from the front plane of the FwEndCap. This value is the same as the distance of the off-point of the subunit to its front face. Figure 7(b) shows the x/y distributions of the points of closest approach.

Orienting the crystals towards a confined region (the off-point region) upstream of the target point prevents photons from passing through the gaps between neighboring crystals and subunits. The distance between the target point and the off-point region is optimized such that photons should cross a gap between crystals within a distance of about 1/3 of the crystal length. This condition has been verified in the simulations and enhances the efficiency of photon detection by the FwEndCap.

3 The FwEndCap simulation results

The simulation studies for the $\overline{\mathrm{P}}$ANDA EMC are focused on the expected performance of the planned EMC with respect to the energy and spatial resolution of the reconstructed photons, on the capability of electron/hadron separation, and also on the feasibility of the foreseen physics program of $\overline{\mathrm{P}}$ANDA [3]. The simulation package contains event generators with proper decay models for all particles and resonances involved in the individual physics channels [14], particle tracking through the complete $\overline{\mathrm{P}}$ANDA detector, a *digitization* procedure which models the signals and the signal processing in the front-end electronics of the individual detectors as well as the reconstruction of charged and neutral particles. In this section, the simulations were performed with photons emitted isotropically from the target point, unless noted otherwise.

3.1 Digitization procedure

The digitization of the EMC has been implemented with realistic properties of PWO crystals at the operational temperature of $-25\,^{\circ}\mathrm{C}$ [3]. A photon entering one crystal of the EMC develops an electromagnetic shower which extends over several crystals. We will refer to a crystal as a *hit* if its signal at the output of the simulation has a non-zero value. Correspondingly, we refer to such a crystal as a *digi* if its signal would pass the digitization procedure (the conversion into electronic signal) in which a minimum *detection threshold* of the order of 2–3 MeV is required. The collection of all the neighboring crystals classified as *digi* is called a *cluster*, where it is possible for a cluster to contain only a single crystal.

Clusters have to be reconstructed with good energy, position, and time resolutions over a wide dynamic range starting from about 10 MeV up to 12 GeV, as expected in the reactions to be studied with $\overline{\mathrm{P}}$ANDA. In these simulations, the statistical fluctuations are estimated, assuming a light yield of 500 photons/MeV for the crystals and a quantum efficiency of 0.7 and 0.22 for the LAAPD and VPTT photo-sensors, respectively [3]. Based on the above-mentioned PWO light yield at the operation temperature, a FwEndCap crystal with the back-face area of $26 \times 26\,\mathrm{mm}^2$ and equipped with a VPTT of $200\,\mathrm{mm}^2$ cathode area would yield 33 photo-electrons/MeV. As this is the worst-case operating condition because of the low quantum efficiency, we adopt this case for the further performance estimates. The signal is convolved with a Gaussian distribution with a standard deviation of $\sigma = 1\,\mathrm{MeV}$ to account for the electronic noise of an individual detector element. This noise level is a conservative estimate based on measurements with a digital readout scheme and digital data treatment [6]. It includes the contributions of the LAAPD excess-noise factor folded with the electronic noise of the preamplifier and readout electronics based on the Sampling ADC (SADC) technique. In the case of VPTT, the noise contribution is dominated by the electronic noise of the preamplifier, yielding about the same performance as the LAAPD readout.

In order to correctly retrieve the crystal position from its row/column number, as indicated by the *hit*, the proper mapping of the geometry has been ensured in the simulations. A monotonous and approximately linear correlation between crystal row number and y-position (or between crystal column number and x-position) of the geometrical center of the crystal was observed which is expected by design of the crystal arrangement in the FwEndCap. Depending on the studied cases, either only the FwEndCap module or the full EMC, including FwEndCap, BwEndCap, and Barrel EMC modules, will be present in the simulated geometry.

3.2 Cluster reconstruction

A photon impinging on the EMC could initiate several (disconnected) clusters. There could be various reasons for the occurrence of disconnected clusters, so-called *split-offs*: migration of a secondary particle, created in one cluster, to another part of the EMC, but not through the crystal material; statistical fluctuations leading to a probability for particles to pass through the crystals without interacting with the bulk of crystals on their way. Also, due to fluctuations in the hadronic and electromagnetic shower-energy distribution, too many clusters may be reconstructed in the EMC, which are not associated with separate primary particles. The shower-shape analysis allows to discriminate such split-off clusters from the photon clusters. One can effectively suppress the split-off clusters by choosing a proper cluster threshold for the physics channel of interest. Although this will be our approach in this paper, there is a need for a more refined algorithm exploiting the threshold dependence.

In general, one can assume two different kinds of split-off clusters: the electromagnetic split-off is a cluster of crystals (usually one) that is located near the primary photon cluster and produced by a shower product (*e.g.* photon) which interacts in a crystal not connected directly to the primary cluster of crystals. The hadronic split-off results in a cluster of crystals (usually very few) produced by some secondary particle (*e.g.* neutrons) due to the interaction of a primary charged particle (π, K) somewhere in the detector. As a result, this type of split-off looks like a photon and perturbs the analysis of events. The characteristics of hadronic split-offs were studied by the Crystal Barrel Collaboration [15]. From these analyses of the hadronic split-offs one can conclude the following:

- They pose a serious problem, since one can expect a 50% chance of split-off per charged hadron.
- Below 20 MeV, hadronic split-offs are very prolific.
- About half of the split-offs are not located near a primary charged-particle track.
- There seem to be no good criteria to flag split-offs.

3.2.1 Cluster position

In this analysis, the FwEndCap is assumed to be the only module present in the simulated geometry. The event analysis is performed only for clusters with highest energy deposition that satisfy a threshold condition of 30 MeV. In sect. 3.2.2 it will be shown that a 30 MeV threshold results in a lower deficit in the number of registered low-energy photons as compared to 1 GeV photons. This threshold value limits the maximum number of registered clusters for 1 GeV photons to 2 per event. Events with two registered clusters comprise only 0.2% of the total number of events for which at least one cluster satisfies the threshold. The x-/y-position of photons hitting the FwEndCap is reconstructed through projecting the reconstructed position of the cluster $\overrightarrow{r}_{cl} = (x_{cl}, y_{cl}, z_{cl})$ along the axis and on the front face of the crystal with the highest deposited energy in the cluster. $\overrightarrow{r}_{cl}$ is defined to have a linear relation with respect to all the *digi* positions ($\overrightarrow{r}_{digi}$). Simulation studies of 1 GeV photons show a mean shower depth of 62 mm, called the *digi* depth-position. The *digi* depth-position is defined as the distance of $\overrightarrow{r}_{digi}$ (the point located on the crystal axis) to the center of the front face of the crystal. This would then give better reconstruction of the impact point of photons than the geometrical center of the crystal (*hit* position). In sect. 3.4, we will use an optimized lookup table to correctly reconstruct the position of the clusters. The obtained value of the *digi* depth position was used as the starting point in the simulations to build this lookup table, which will then take care of the deviations for various photon energies. The look up table will eventually absorb irregularities like the shower leakages as well as the assumed crystal properties like non-uniformity in the light collection, the *digi* threshold, and the *digi* depth position. The simulation analysis shows that the position reconstruction in the FwEndCap gets worse when one uses a linear energy weighting instead of a logarithmic one. This is shown to be more crucial for 1 GeV as compared to 100 MeV photons. The position of the cluster $\overrightarrow{r}_{cl}$ is thus obtained through a logarithmic rather than a linear energy weighting formula. This ansatz is motivated by the fact that the shower profile has an exponentional shape. Hence, every individual crystal with E_{digi} energy deposition belonging to a cluster with an energy content of E_{cl} would contribute a positive weight of W_{digi} in the position reconstruction as $W_{digi} = W_0 + \ln(E_{digi}/E_{cl})$, where W_0 would control the smallest fractional energy that a crystal can have and still contribute to the position measurement. As W_0 decreases, the modules with the highest energy are weighted more heavily, while modules having an energy fraction below $\exp(-W_0)$ are excluded entirely. Therefore, if W_0 is too small, only a few modules dominate the position calculation and the results become sensitive to the position of incidence and the distribution of the position difference becomes non-Gaussian [16]. For instance, for $E_{cl} = 30$ MeV (100 MeV), only a $W_0 \geq 2.3$ (3.5) guarantees that contributions of crystals with $E_{digi} \geq 3$ MeV will be taken into account in the position reconstruction of the cluster. A $W_0 = 2.3$ (3.5) means that only crystals in the cluster containing more than 10% (3%) of the cluster energy will contribute to the position measurement. In the PandaROOT package, the functional form of W_0 has been taken to be the same as was used by the BaBar experiment [17],

$$W_0 = A - B \cdot \exp(-C \cdot E_{cl}). \quad (1)$$

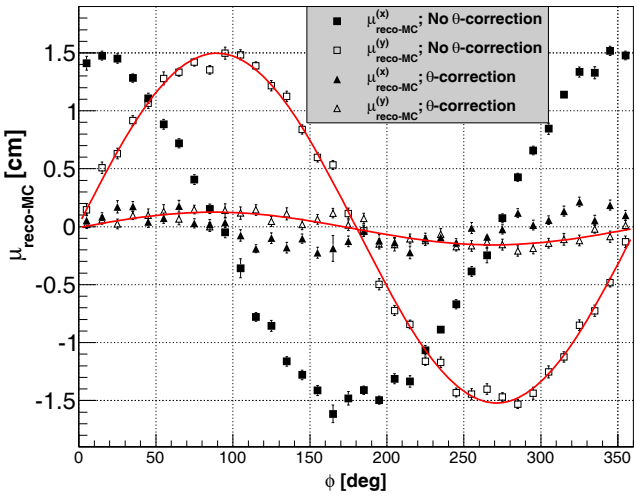

Fig. 8. The mean value ($\mu_{reco-MC}$) of the Gaussian fit to the histogram $y_{cl} - y_{MC}$ (or $x_{cl} - x_{MC}$) for the cluster with highest energy deposition per event which satisfies the threshold condition of 30 MeV. A and B in eq. (1) are assumed here to be 3.8 and 0, respectively, and the isotropically generated photons of 100 MeV scan over the FwEndCap. The error bars are the fit errors of the mean values. The curves are sinusoidal fits to the data; the data are shown for cases with or without using the lookup table for the correction of the θ-angle.

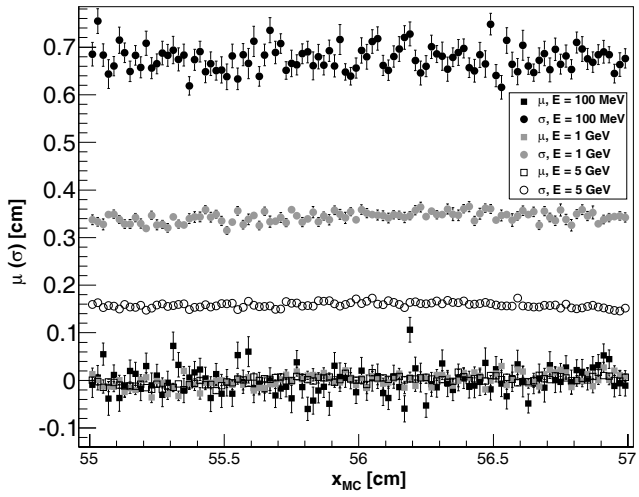

Fig. 9. The mean (μ) and standard deviation (σ) of the Gaussian fit to the histogram $y_{cl} - y_{MC}$ for the cluster with highest energy deposition per event which satisfies the threshold condition of 30 MeV. Here, the isotropically generated photons of 100 MeV, 1 GeV, and 5 GeV scan over a region covering the gap between two neighboring subunits ($x \approx 56$ cm).

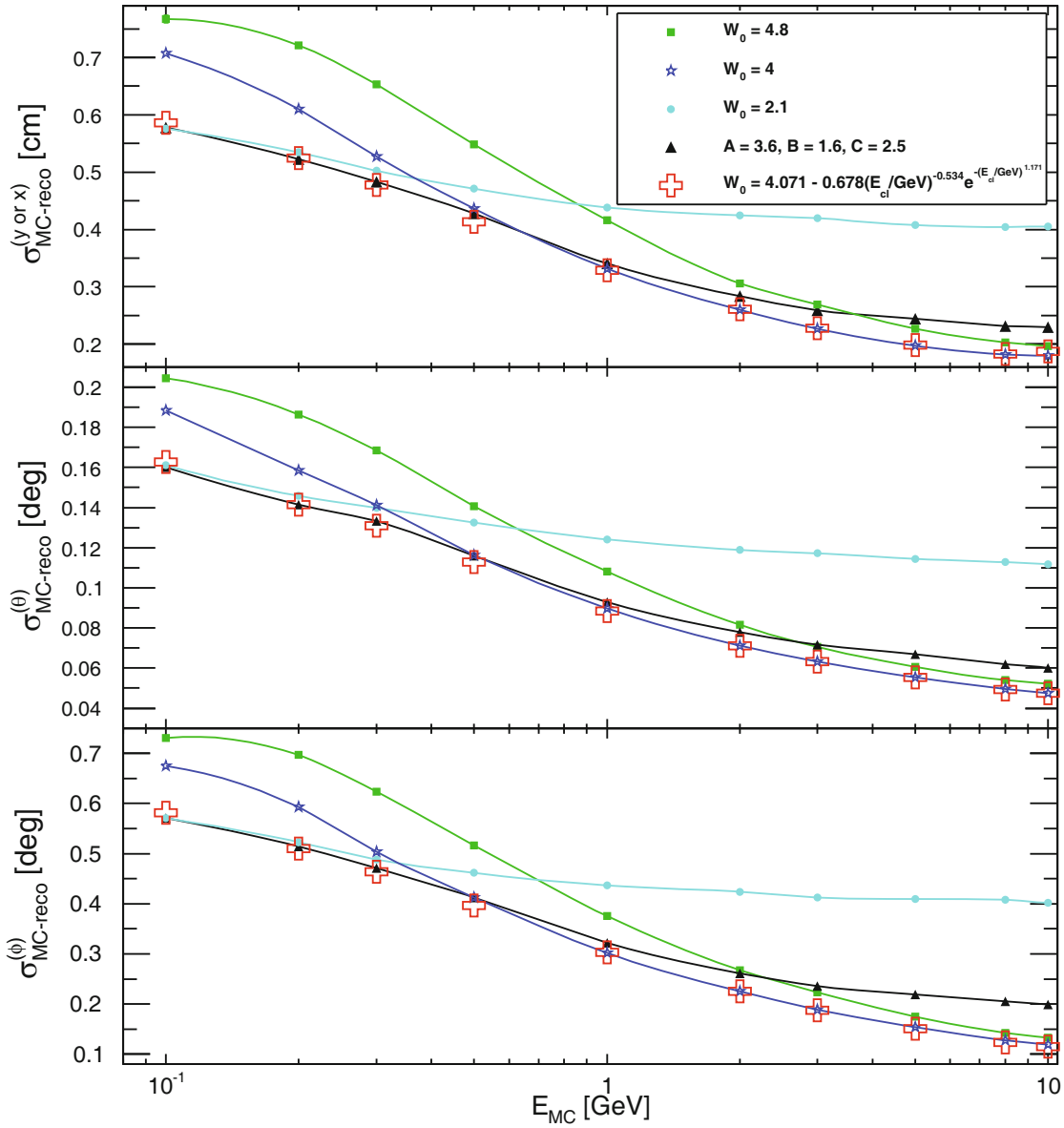

Fig. 10. Simulation results for the $\sigma = \mathrm{FWHM}/2.35$ of the difference between the reconstructed and Monte Carlo values of the x-/y-position (top panel) and the θ-/ϕ-angle (bottom panels) of the registered clusters in the FwEndCap as a function of the photon energy. Data are provided for various values of W_0 as well as one set of the parameters A, B, and C that are related to a logarithmic weighting for position reconstruction, as introduced in eq. (1). The hollow pluses show the results taking eq. (3) as the functional form for W_0. The error bars show the statistical uncertainty and are barely visible. The photons are generated within $\theta = 15°$–$18°$ over the FwEndCap. A smooth line is drawn through each data set to guide the eye.

If we had more than one *digi* (crystal) in the cluster, the cluster position would be

$$\vec{r}_{cl} = \frac{\sum_{digi} W_{digi} \cdot \vec{r}_{digi}}{\sum_{digi} W_{digi}} . \qquad (2)$$

In reconstructing the position of the photons, there is a ϕ dependence observed for the mean values $\mu_{reco-MC}$ of the deviation between reconstructed and MC-true positions, expressed by Gaussian fits to the histograms $y_{cl} - y_{MC}$ and $x_{cl} - x_{MC}$. This ϕ dependence of sinusoidal shape (see fig. 8) is a geometrical effect because the off-point and the target point do not coincide. Since the off-point is located about 1 m upstream of the target point, most photons generated at $\phi \approx 0°$, cause a horizontal rather than a vertical shift of the shower position. This effect would correspond to a minimum (maximum) expected value for $|y_{cl} - y_{MC}|$ at $\phi \approx 0°$ ($\phi \approx 90°$). Similarly, based on symmetry arguments, we should observe a minimum (maximum) expected value for $|x_{cl} - x_{MC}|$ at $\phi \approx 90°$ ($\phi \approx 180°$), which ensures the sinusoidal behavior.

Due to the fact that the off-point and target point do not coincide, a lookup table has been exploited for the correction of the cluster θ-angle that is derived from the Monte Carlo studies. The reconstruction of the cluster position shows clear improvement when the cluster θ angle is corrected by the lookup table. This lookup table will be discussed in sect. 3.4 along with the lookup table for the energy correction. For the rest of the discussion we apply this correction. The residual deviation of the corrected mean difference $\mu_{reco-MC}$ in fig. 8 (100 MeV photons) from the zero level amounts to a small uncertainty in the position resolutions that will be presented below. This is calculated to be about 0.1 mm, 0.13 mm, and 0.2 mm for photon energies of 100 MeV, 1 GeV, and 5 GeV, respectively.

For various photon energies, fig. 9 shows the mean (μ) and standard deviation (σ) of the Gaussian fit to the histogram $y_{cl} - y_{MC}$ for the cluster with highest energy deposition per event which satisfies the threshold condition of 30 MeV. Photons are generated over $15° < \theta_{MC} < 16°$ and $7° < \phi_{MC} < 10°$. This solid-angle range allows for scanning a region covering the gap between two neighboring subunits. This is the gap between the crystal columns #22 and #23, which is located at $x = 56$ cm. x_{MC} and y_{MC} are the coordinates of the entrance point of the photon to the front face of either of the two neighboring crystals that is under scanning. The scanning steps in the x-direction are taken to be 0.2 mm, whereas the thickness of the alveole between the two subunits is 0.36 mm. The continuity of x_{MC} dependence of the resolution results (σ in fig. 9) demonstrates that there will not be local inhomogeneities that could introduce fluctuations in the position resolutions for individual photons.

In the PandaROOT simulations of the FwEndCap, we optimized the parameter A in eq. (1) for a few values of B and C, and for the energy range from 100 MeV to 10 GeV. The sensitivity of the simulations was checked by allowing A to change from 2 to 5 in steps of 0.1 as well as from 6 to 10 in steps of 1. For instance, for $C = 2.5$ and $B = 1.6$, the sensitivity was checked resulting in the optimized value for A of 3.6. Figure 10 compares the corresponding resolution results with the ones derived assuming energy-independent W_0 values. The resolution results are limited to a central region of the FwEndCap, where there is little chance for shower leakage from the boundaries of the FwEndCap. Thus, we observe the intrinsic resolution while distorting effects have to be taken into account lateron. One can see from eq. (1) that, as the energy increases, the exponential term diminishes the contribution of the parameter B. In optimizing these parameters for various modules of the EMC, one notices that the influence of B and C would become appreciable for the low energy clusters. In principle, one needs to find the optimized values of B and C in conjunction with A if one employs the parameterization of eq. (1). Alternatively, one can assume an energy-dependent $W_0(E_{cl})$ and try to find its functional form by allowing W_0 to vary within a reasonable range. Figure 11 shows the optimized W_0 derived for the FwEndCap as a function of the cluster energy. For

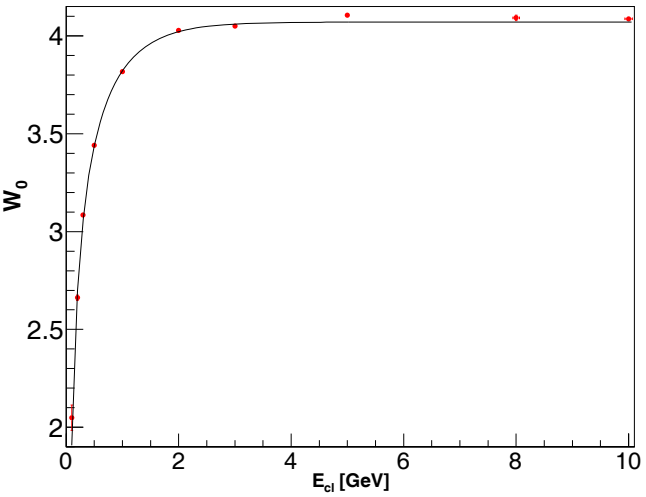

Fig. 11. Optimized W_0 derived for the FwEndCap as a function of cluster energy. The curve is a fit with the functional form given in eq. (3). The horizontal error bars that are barely visable indicate the σ = FWHM/2.35 of the difference between the photon energy and the reconstructed energy of the cluster with highest deposited energy. The value of the optimized W_0 was taken as the one corresponding to the minimum resolution by fitting the resolution as a function of W_0. The error size of W_0 was calculated from the fit, taking into account the χ^2 of the fit for each energy. The reduced χ^2 of the fit in this figure is 4.54.

each photon energy, W_0 was changed between 2 and 5 in steps of 0.05 and the optimized value of W_0 was chosen to be the one that resulted in the best position resolution of the cluster with highest deposited energy. Using this $W_0(E_{cl})$ function for the FwEndCap in the absence of any potential non-uniformity in the light yield, the resolution results are presented in fig. 10 (hollow pluses). These results suggest the following parametrization, obtained by a fit with $\chi^2_R = 4.54$, for the logarithmic energy weighting to be used for the FwEndCap instead of eq. (1):

$$W_0 = 4.071 - 0.678 \times \left(\frac{E_{cl}}{\mathrm{GeV}}\right)^{-0.534} \cdot \exp\left(-\left(\frac{E_{cl}}{\mathrm{GeV}}\right)^{1.171}\right). \quad (3)$$

The x-/y-position uncertainties in fig. 10 appear to be small compared to the width (24.37 mm) of the front face of the crystals. The reason for a worse resolution in the ϕ reconstruction than in the θ reconstruction is an average lower number of crystals per unit ϕ-angle than per unit θ-angle. These angular resolutions should be compared with the angular coverage of a single crystal seen from the target point, which varies, for different crystals of the FwEndCap, within the ranges $0.6° < \Delta\theta < 0.7°$ and $1° < \Delta\phi < 7°$ along the θ- and ϕ-direction, respectively.

Figure 12 shows the reconstructed versus Monte Carlo mean values of the photon position for nine equidistant coordinates of impact along the y-axis on the face of the crystal. The results are shown for five photon energies, to be representative of typical low- and high-energy pho-

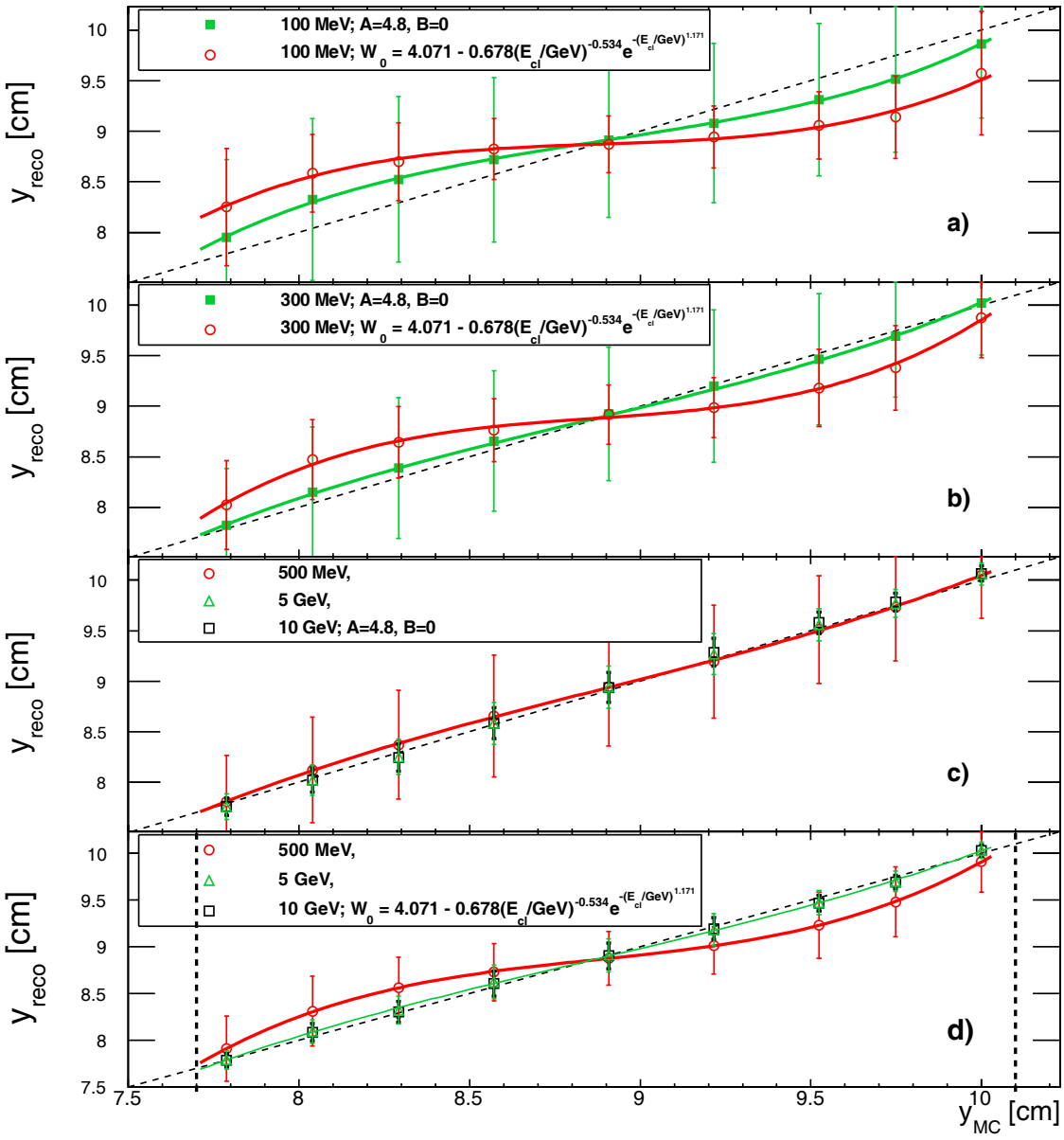

Fig. 12. The reconstructed mean values versus Monte Carlo values of the photon position for nine equidistant hitting points along the y-axis at the mid-x on the face of the crystal located at (row = 4, column = 25). The vertical dashed lines mark the left and right edges of the front face of the crystal. The error bars are the standard deviation of the reconstructed y-position. The data are for five photon energies, one set of parameters in eq. (1) (panels a-c) and the parametrization in eq. (3) (panels a, b, and d). The curves are fits to the data points.

tons in the $\overline{\mathrm{P}}$ANDA experiment, and one set of parameter values in eq. (1) ($A = 4.8$ and $B = 0$). The FwEndCap analyses showed that the closest mean values of the reconstructed x-/y-position to the diagonal line in fig. 12 would correspond to $A = 4.8$ and $B = 0$. This is checked to be the case for various photon energies. As the photon energy increases, the curved function fitted to the mean values tends to become straight along the diagonal line. However, the error bars are considerably larger than those derived from eq. (3) (compare, for instance, fig. 12 (a) and (b)), in accordance with the corresponding resolutions shown in fig. 10. For high-energy photons of 10 GeV, as opposed to an energy of 5 GeV, the smaller size of the error bars in fig. 12 ensures higher resolutions in fig. 10.

3.2.2 Cluster multiplicity

In this analysis, the FwEndCap module is embedded in the full EMC geometry. Figure 13 shows the sensitivity of the *digi* multiplicity distribution to various detection thresholds for photons of 100 MeV, 500 MeV, and 1 GeV energy.

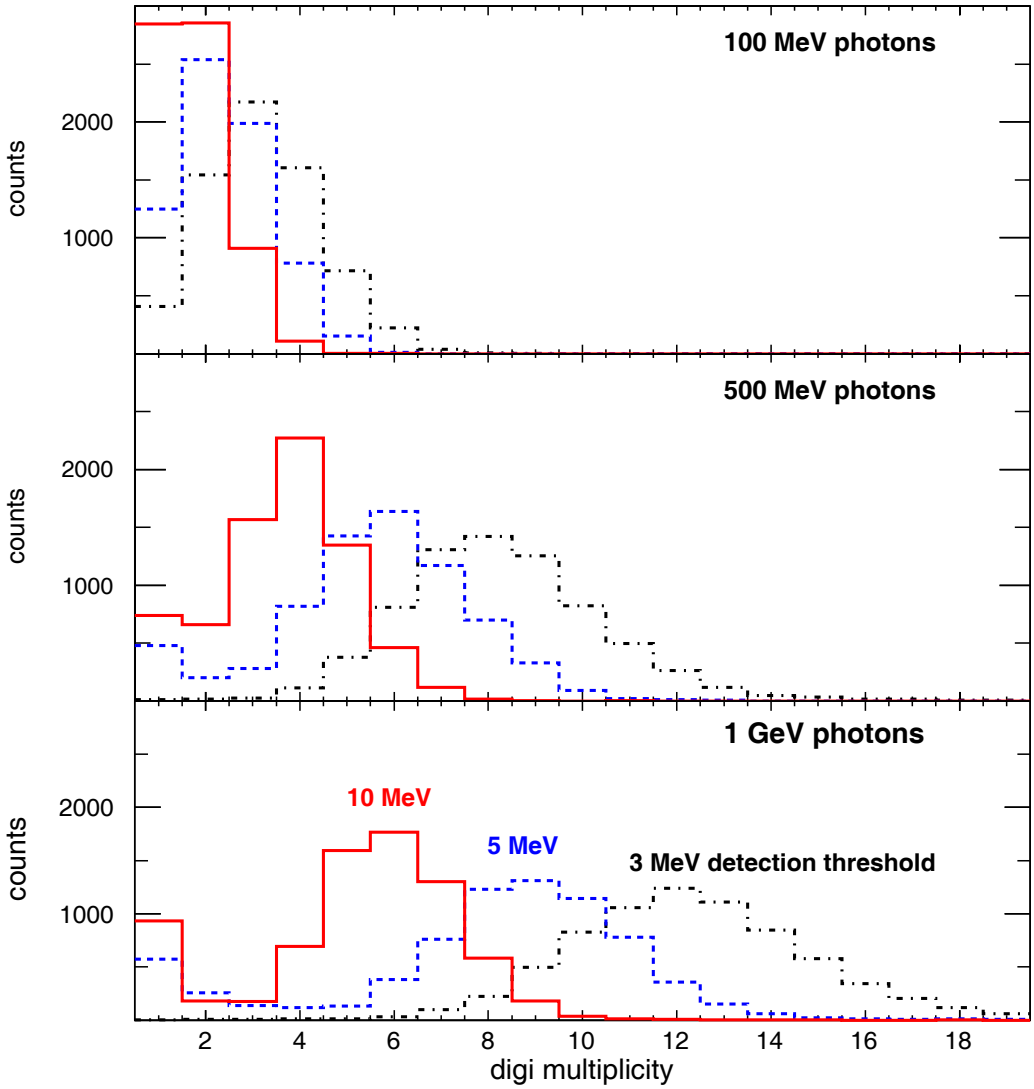

Fig. 13. Sensitivity of the *digi* multiplicity distribution in the FwEndCap module to various detection thresholds of 3 MeV (dash-dotted), 5 MeV (dashed blue), and 10 MeV (solid red histograms) for 100 MeV (top panel), 500 MeV (middle panel), and 1 GeV (bottom panel) photons emitted into the full EMC.

Table 1. The mean N of the *digi* multiplicity distributions shown in fig. 13 for various detection thresholds and photon energies. In addition to fig. 13 the mean values for the 0 MeV detection thresholds are also shown here.

Photon energy [MeV]	N For detection threshold [MeV]			
	0	3	5	10
100	6.1	3.2	2.4	1.7
500	16.1	8.3	5.6	3.7
1000	23.2	12.6	8.1	5.3

The mean values N of the *digi* multiplicity distributions are summarized in table 1. In the case of a 0 MeV detection threshold, the mean *digi* multiplicity increases significantly. The relatively high number of events with one *digi* per event, as compared to two or three *digi*s per event, for the multiplicity patterns of 5 and 10 MeV detection thresholds in the lower two panels of fig. 13, reflects the fact that a considerable number of the FwEndCap crystals close to the circumference are screened against direct impact of photons by the forward edge of the Barrel EMC (see fig. 6). This overlap is intended in order to guarantee a complete coverage for photon detection. High-energy photon showers that partially leave the forward edge of the Barrel EMC would mostly cause one-*digi* clusters in the FwEndCap for detection thresholds above 3 MeV. On the other hand, photons that directly hit the FwEndCap would cause a Poissonian *digi*-multiplicity distribution. The pattern that we observe in the lower panel of fig. 13 for the 10 MeV detection threshold is a superposition of the Poissonian and the one-*digi* distributions.

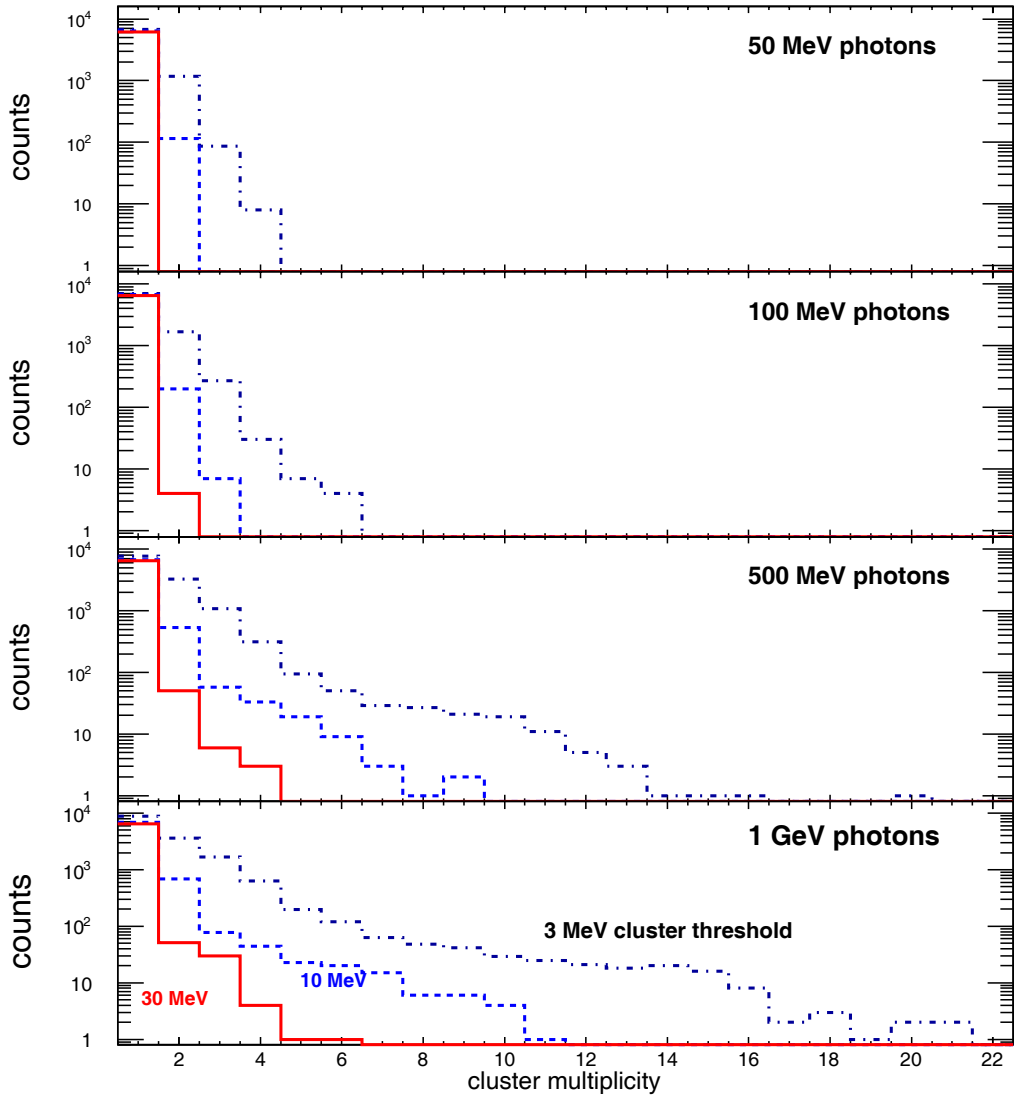

Fig. 14. Cluster multiplicity distributions in the FwEndCap for various cluster thresholds of 3 MeV (dash-dotted black), 10 MeV (dashed blue), and 30 MeV (solid red histograms) for photons of 50 MeV, 100 MeV, 500 MeV, and 1 GeV energy. Here, the digitization detection threshold is 3 MeV.

Figure 14 shows the multiplicity of clusters for the FwEndCap module, assuming various cluster thresholds for 50 MeV, 100 MeV, 500 MeV, and 1 GeV photons emitted into the full EMC geometry. As mentioned in sect. 3.2.1, if the FwEndCap is the only module present in the simulated geometry, we would expect for 1 GeV photons and a 30 MeV detection threshold a maximum of two clusters per event, where about 0.2% of the events contain 2 clusters. In the corresponding cluster multiplicity distribution of fig. 14 for the full geometry, the percentage of events with 2 clusters is 0.8% due to the effect of the forward edge of the Barrel increasing the cluster multiplicity in the FwEndCap. We have checked for the optimum value of the cluster threshold energy (as far as the efficiency is concerned), by comparing the results for 50 MeV, as representative for low-energy photons, with the ones for 1 GeV photons. For various cluster thresholds, we studied the ratio of the number of events with cluster multiplicity of 1 for 50 MeV photons to the number of events with cluster multiplicity of 1 for 1 GeV photons. Table 2 summarizes the obtained simulation results for the FwEndCap as part of the full EMC module. It shows that, assuming a 30 MeV rather than other cluster thresholds, one would expect a lower deficit in the number of the registered low-energy (say, 50 MeV) photons as compared to 1 GeV photons.

Table 2. Simulation results of the FwEndCap, as part of the full EMC module, showing the decrease in the percentage of events with cluster multiplicity of 1, when comparing 50 MeV with 1 GeV photons.

Cluster threshold [MeV]	10	20	30	35	40
Registered event deficit [%]	7	4.7	4.5	6.1	12.3

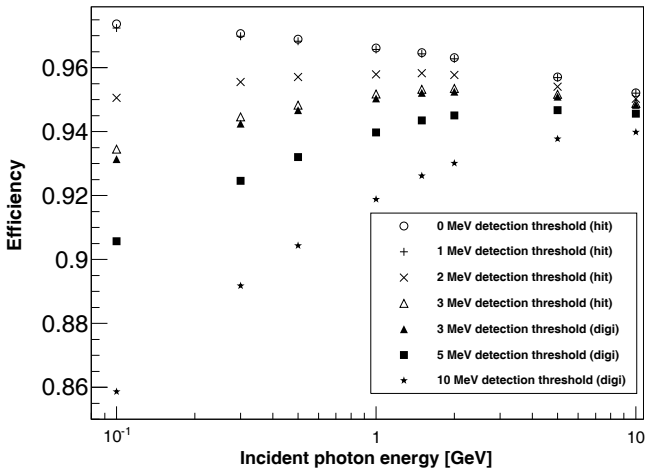

Fig. 15. The full-energy efficiency of the sum of energy depositions in the FwEndCap as a function of the thrown photon energy, for photons emitted isotropically from the target point. For the analysis based on the *hit* information, the results are presented for detection thresholds of zero (circles), 1 MeV (plus symbols), 2 MeV (cross symbols), and 3 MeV (hollow triangles). For the analysis based on *digi* information, the results are presented for detection thresholds of 3 MeV (solid triangles), 5 MeV (squares), and 10 MeV (stars).

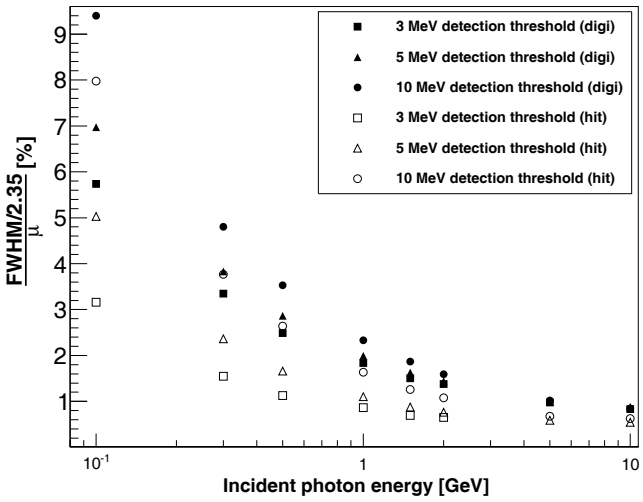

Fig. 16. Simulation results for the energy resolution of the FwEndCap as a function of the incident energy of photons. The simulations are performed for detection thresholds of 3, 5, and 10 MeV at *hit* and *digi* levels. FWHM and μ on the y-axis represent the full width at half maximum and the peak position, respectively, of the Lorentzian fit function to the total energy deposition registered by the crystals. In these simulations a uniform light collection efficiency at various interaction points along the length of the crystals is assumed.

3.3 Efficiency and energy resolution for photons

In this subsection, the simulated geometry contains only the FwEndCap module in order to evaluate its performance in photon detection without effects of neighbouring detector components.

3.3.1 Full-energy efficiency

Since electromagnetic showers could leak out of the FwEndCap, thereby losing part of the energy of the impinging photons, we performed a number of simulations to obtain the average collected energy for various photon energies.

Figure 15 shows the *full-energy efficiency*, *i.e.* the fraction of the full energy registered by those crystals which satisfy the detection threshold. We expect a considerable fraction of energy leaking out for hitting points close to the edges of the FwEndCap. This explains why we see, on average, 3% loss in the efficiency even at very low energies for the threshold-free case. In a threshold-free situation (circles), detectors fully register the deposited energies and, hence, the average percentage of the total registered energy would decrease with increasing photon energy due to the increase in shower leakage from the edges. This decreasing trend persists even when we introduce a 1 MeV threshold for the crystals (plus symbols), but starts to change already as we approach a 2 MeV threshold (cross symbols). The reason for this change of trend is that at lower energies, say 0.1 GeV, a higher percentage of incident energy is not registered due to the threshold condition. At a higher photon energy, say 0.3 GeV, a lower percentage of the incident energy would be lost due to non-firing crystals. Therefore, for thresholds higher than about 2 MeV, the overall curve of the full-energy efficiency rises with increasing photon energy and then drops, as can be seen for various detection thresholds in fig. 15. The reason for the subsequent decrease of the efficiency is that for photons with high enough energy the leakage of energy from the edges of the FwEndCap would dominate over the aforementioned threshold effect. The various efficiency curves tend to approach each other, as the photon energy increases, due to the dominant impact of the energy leakage in determining the full-energy efficiency. Also, the impact of noise diminishes, as is observed for the *hit* and *digi* curves for 3 MeV detection threshold, which smoothly coincide as the energy increases.

3.3.2 Energy resolution

Figure 16 shows the simulations for the energy resolution of the FwEndCap calorimeter for various detection thresholds at *hit* and *digi* levels. The *hit* and *digi* concepts were explained in sect. 3.1, where a *digi* was defined as a *hit* satisfying a certain threshold energy in the presence of noise. Clearly, increasing the detection threshold drastically worsens the resolution, especially as we approach the lower photon energies. This reflects the pattern observed in fig. 15 and implies that the detection threshold appears

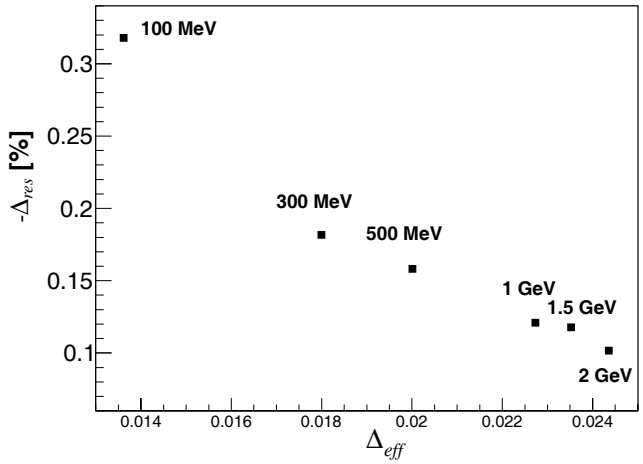

Fig. 17. The difference in the energy resolution ($-\Delta_{res}$) as a function of the difference Δ_{eff} in full-energy efficiency for the two cases of the average over the FwEndCap and a well-defined cluster position inside the FwEndCap. The central crystal of the cluster is located at (row = 2, column = 19). In these simulations a 3 MeV *digi* threshold is assumed. The data points correspond to photon energies of 100, 300, 500, 1000, 1500, and 2000 MeV.

to be highly influential on the quantities of interest such as the full-energy efficiency as well as the energy resolution. On the other hand, by increasing the photon energy, the effect of the detection threshold (in the order of 10 MeV) on estimating the resolution fades away; in the case of 5 and 10 GeV photons, the estimated *digi* resolutions practically coincide for the three detection thresholds 3, 5, and 10 MeV. It is also worth noting that *hit* and *digi* resolution curves seem to approach each other, as we increase the photon energy. The relative energy resolution is conventionally described by $\frac{\sigma}{E} = a \oplus \frac{b}{\sqrt{E}} \oplus \frac{c}{E}$ [18] with the constant instrumental term, the stochastic term, and the noise term weighted by the parameters a, b, and c, respectively. The stochastic term includes intrinsic shower fluctuations, photo-electron statistics, dead material at the front of the calorimeter, and sampling fluctuations. The noise term includes contributions from the readout electronics noise whose contribution to the standard deviation σ does not depend on energy. The constant term includes non-uniformities in signal collection and the possible error in the detector calibration. The symbol $\oplus$ represents addition in quadrature. At high photon energies, the contributions of the two energy-dependent terms would approach zero, which explains why the *hit* and *digi* data would effectively be the same at high enough photon energies and given by the constant term a. In order to check for systematic variations due to the edge effects, we choose a well-defined cluster (index *cluster*) inside the FwEndCap and compare the response in energy resolution (FWHM) and full-energy efficiency (ϵ) with the average over the FwEndCap. To this end we simulate an isotropic photon distribution (index *average*) and define the following differences:

$$\Delta_{res} = \left(\frac{FWHM}{2.35\mu}[\%]\right)_{cluster} - \left(\frac{FWHM}{2.35\mu}[\%]\right)_{average}$$
$$\Delta_{eff} = \epsilon_{cluster} - \epsilon_{average}, \quad (4)$$

for the differences in energy resolution and full-energy efficiency, respectively. For various photon energies, fig. 17 shows the correlation between Δ_{res} and Δ_{eff}. The fact that 2 GeV photons have the largest change in efficiency and the smallest change in resolution confirms that the energy leakage from the FwEndCap edges is larger at 2 GeV than at the lower photon energies. At the lower photon energy of 100 MeV, the energy leakage is small and causes little change in the full-energy efficiency but the impact of edge leaking on the energy resolution is large.

3.3.3 Light-yield non-uniformity

In the simulations of figs. 16 and 17, a uniform light transport is assumed as a function of the distance of the interaction point to the photo-sensor. In reality, however, non-uniformities may occur due, for instance, to the crystal geometry and one needs to validate the simulations by extracting the non-uniform light attenuation and light collection from prototype experiments. It has been shown that a stable temperature is of utmost importance in keeping a uniform detector response for PWO crystals [19]. Contributions to the non-uniformity for both tapered and non-tapered crystals originate from light attenuation along the crystal due to intrinsic absorption inside the material, reflective properties of the crystal surface, transmission through the surface, the wrapping material as well as from diffusion on impurities and bubbles. In general, light collection of the full-size PWO crystal is a result of the interplay of optical absorption and focusing effect. Non-tapered crystals have the same value of the light yield along the length, because the focusing effect is negligible.

Based on the analysis of an array of 10×6 Barrel-type crystals in the PROTO60 experiment [6] and the comparisons with simulations, we could derive the non-uniformity from the data. In the simulations, the non-uniformity is implemented and calculated at the level of the interaction point where some energy is deposited. The procedure makes sure that only a specific percentage of this deposited energy will be taken into account depending on the distance of the interaction point to the face of the crystal. For instance, introducing an overall 30% linear non-uniformity means that 100%, 85%, and 70% of the deposited energy is collected, respectively, for an interaction point located at the front face, middle, and the back face of the crystal. The analyses were performed for a 3×3 crystal configuration in which every crystal was equipped with one LAAPD photo-sensor of $10 \times 10\,\mathrm{mm}^2$ area yielding a sensitivity of 52 photo-electrons/MeV. In the experiment, bremsstrahlung photons produced by an electron beam were collimated and focused at the center and perpendicular to the front face of the central crystal. The digitized

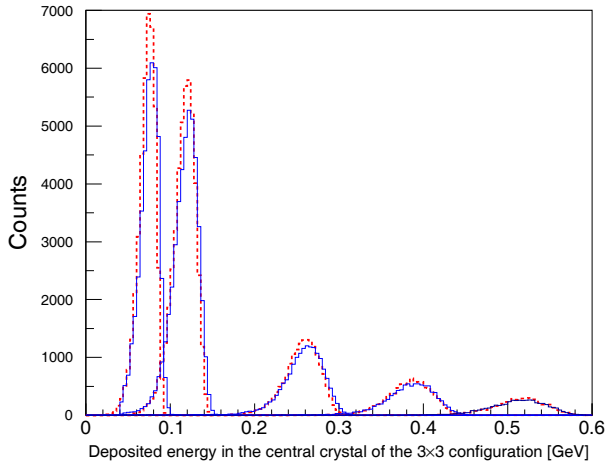

Fig. 18. The superimposed spectra at five photon energies comparing simulations for a light yield of 500 photons/MeV, a zero noise level, and a 1.5%/cm linear non-uniformity (red dashed-histogram) and experimental data (blue solid histogram). The spectra show the deposited energy in the *central* crystal of the 3×3 crystal configuration of PROTO60 at photon energies of 93.97, 152.72, 339.67, 509.88, and 685.58 MeV. The absolute energy scale was normalized to the simulation at 685.58 MeV.

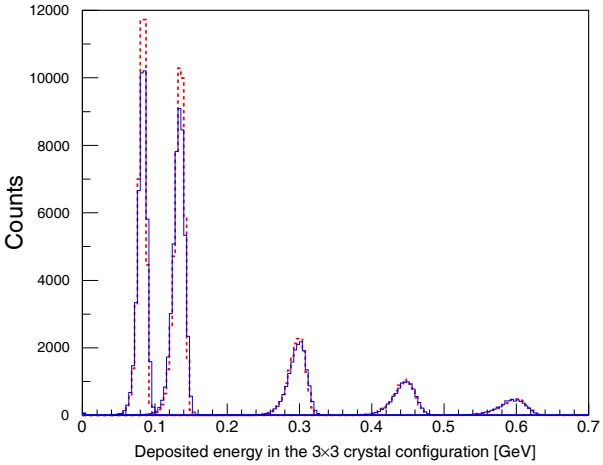

Fig. 19. Same as fig. 18, but showing spectra of the deposited energy in the 3×3 crystal configuration of PROTO60.

data were obtained having a 2 MeV threshold and using the readout electronics based on the SADC. The values of the noise and non-uniformity parameters have been extracted by comparing simulations and data for a grid of values of non-uniformity and noise. A non-uniformity in the light yield, decreasing linearly by 1.5%/cm from the entrance to the photo-sensor face of the crystal, could explain the peak positions simultaneously in the energy-deposition spectra of the central crystal in a cluster as well as the energy sum of the nine crystals over a certain energy range. Figure 18 compares the superimposed spectra of the resulting simulations and the experimental data for five photon energies. The spectra show the deposited energy in the central crystal of the 3×3 crystal configuration of PROTO60. Figure 19 compares, for the same photon energies, the simulations and experimental data for the deposited energy in the 3×3 crystal configuration of PROTO60. The simulated spectra of figs. 18 and 19 contain the same number of events as the experimental spectra at the respective photon energy. Figures 18 and 19 are obtained, assuming a light yield of 500 photons/MeV and a zero noise level in the simulations of the detector response. This low noise level is in accordance with the digital analysis of the PROTO60 data [6] and the parameterization of the energy resolution where the noise term is found to be absent [20]. Adopting these parameters, we compared the energy resolutions obtained in the simulations with the PROTO60 experiment. Figure 20 shows the resolution as a function of energy for the 3×3 crystal configuration with a 2 MeV detection threshold for each crystal. Different simulations were performed for different values of the noise level and light yield, in order to check the sensitivity of the resolutions to these parameters. The optimized values for the noise level and light yield were obtained to be 1.5 MeV and 500 photons/MeV, respectively. These parameters together with the 1.5%/cm linear non-uniformity will be used in sect. 4 for the Barrel crystals to study the detector performance for a benchmark physics channel. Experimental studies of the End-cap crystals have shown no indications of non-uniformity in the light yield of these crystals [21].

3.4 Cluster energy correction

In the process of reconstructing and retrieving the correct energy and direction of the photons in the simulations, we used an optimized lookup table as a function of the cluster energy and polar angle. Cluster energies need to be corrected, in order to take into account the energy losses due to leakage and energy thresholds for single crystals. In order to construct the lookup table for the energy-angle correction of the clusters, simulations were performed with photons emitted isotropically from the target point at energies distributed uniformly between 2 MeV and 10 GeV. This energy range is large enough to include even the highest energy gammas expected in the study of the physics channel of interest that will be discussed in sect. 4. A two-dimensional histogram was filled in (E_{cl}, θ_{cl}) bins for each cluster at a certain polar angle θ_{cl} and energy E_{cl}. The assigned energy E_{cl} was taken from the predefined PandaROOT function for retrieving the deposited energy of the cluster without any correction. This function returns the total energy of *digi*s in the cluster. The weight for filling a certain 2D bin was defined by the ratio of the Monte Carlo energy of the generated photon and the retrieved energy of the cluster with highest deposited energy. This was invoked to minimize the contribution of split-off clusters such that the direction of the reconstructed cluster is close to the direction of the photons generated in the Monte Carlo simulations. Finally, the energy correction value corresponding to each bin is taken to be the mean value of the bin content. This is also the case for

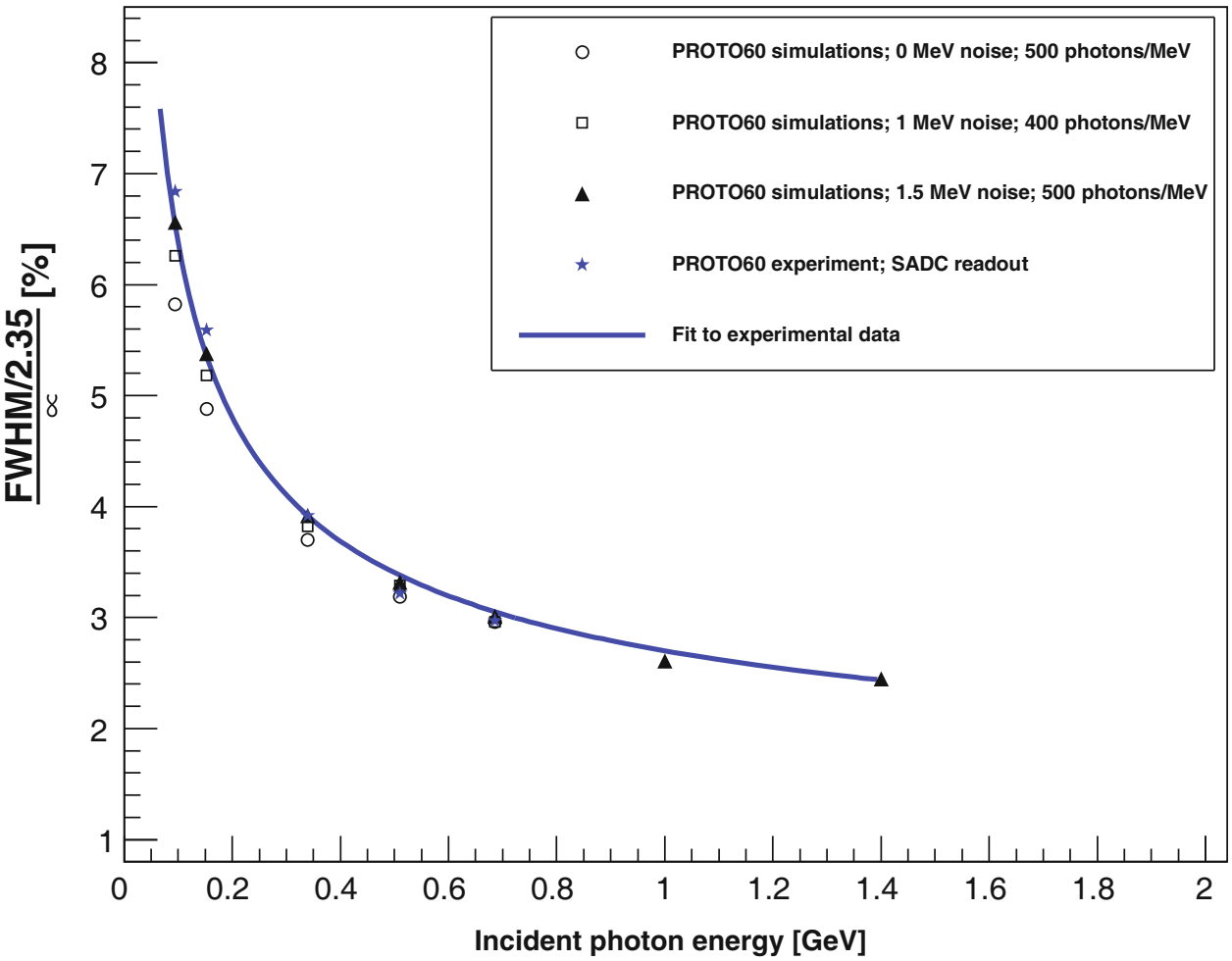

Fig. 20. Simulation results (triangles, squares, and circles) for the energy resolution of the PROTO60 experiment (blue stars). The data and simulations are shown for the 3×3 crystal configuration with a 2 MeV detection threshold. The solid curve represents a fit to the data with the functional form of $1 + \frac{1.7}{\sqrt{E}}$ [6], where the constant 1 arises from uncertainties in the cross-calibration of the nine crystals. This function is in agreement with the fit according to $1.95 \oplus \frac{1.9}{\sqrt{E}}$ within the error bars. Generally, a linear non-uniformity of 1.5%/cm is introduced.

the direction (θ) correction which is taken as the difference between the Monte Carlo and reconstructed angle of the cluster with highest deposited energy. In practice, the lookup table for correcting the cluster energies needs to incorporate the found non-uniformity of 1.5%/cm for the Barrel crystals. In the following we will make use of the obtained lookup table whenever we refer to cluster energies.

4 Charmonium h_c analyses

4.1 Cluster energy and multiplicity

One of the goals of the $\overline{\text{P}}$ANDA physics program is to measure the mass and the width of charmonium states with a resolution of 50–100 keV. Charged reaction products together with photons are to be measured and analyzed. For the charmonium $h_c(1P)$ state, with the mass of $3525.31 \pm 0.11(\text{stat.}) \pm 0.14(\text{syst.})\,\text{MeV}/c^2$ and a width of $\Gamma = 0.7 \pm 0.28 \pm 0.22\,\text{MeV}$ [22], various decay modes can be investigated such as $J/\psi\pi\pi$, $\pi^+\pi^-\pi^0$, $2\pi^+2\pi^-\pi^0$, $3\pi^+3\pi^-\pi^0$, and $\eta_c\gamma$. Among these, the latter two have been observed [18]. In order to test the performance of the $\overline{\text{P}}$ANDA calorimeter, a simulation study was performed for the representative decay channel $\overline{p}+p \to h_c \to \eta_c+\gamma \to (\pi^0+\pi^0+\eta)+\gamma \to 7\gamma$. Thus, in the final state, we would have 7 photons to be detected by the $\overline{\text{P}}$ANDA detector and to be used to reconstruct the invariant mass of final-state mesons and the h_c resonance.

Figure 21 shows Monte Carlo results for the relation between various kinematical variables of the two decay products of the h_c in $p\overline{p}$ annihilation, namely the transition γ and the η_c assuming the $\sin^2(\theta_{CM})$ decay angular distribution from [23]. The mass of the h_c was taken to be $3525.3\,\text{MeV}/c^2$, the width 0.7 MeV. The sensitivity of the kinematical variables to the width of the h_c, about

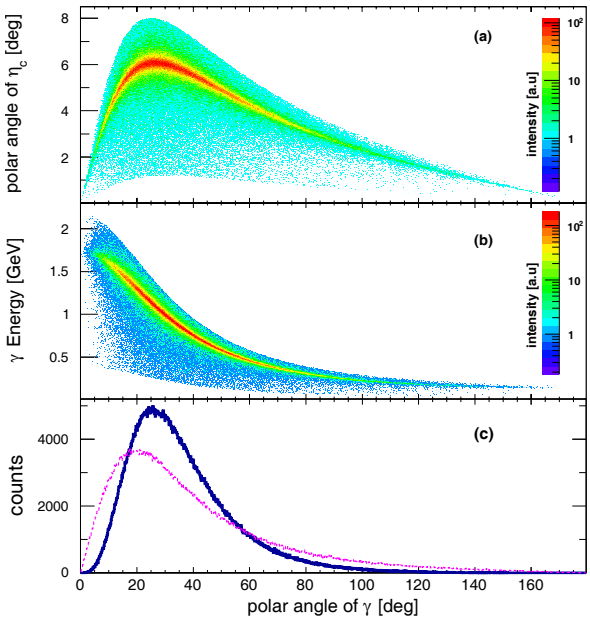

Fig. 21. Monte Carlo simulations of kinematical variables in the laboratory system for h_c production in $p\overline{p}$ annihilation and the decay channel $h_c \to \eta_c + \gamma$ assuming the $\sin^2(\theta_{CM})$ decay angular distribution from [23]. The beam energy was tuned to the production threshold energy of 6.6231 GeV. (a) polar scattering angle of η_c as a function of the angle of the transition γ; (b) energy of the transition γ as a function of its scattering angle; (c) solid blue histogram: distribution of the scattering angle of the transition γ; dashed magenta histogram: same for the 6 γ generated in the π^0 and η decays as well as the transition γ when generated in the phase space decay of the h_c.

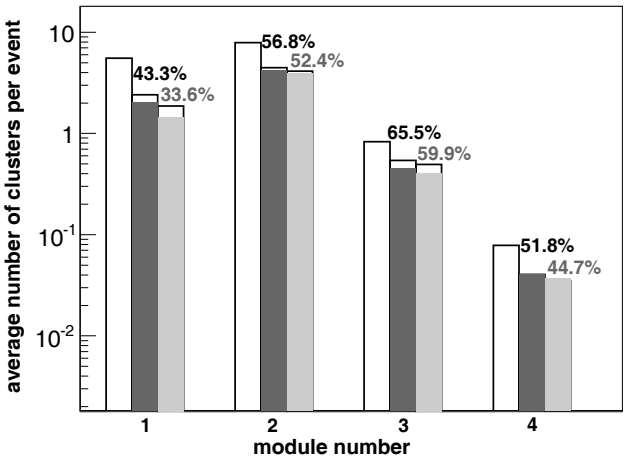

Fig. 22. Simulation results for the average number of clusters per h_c decay in the four EMC modules: FwEndCap (1), Forward Barrel (2), Backward Barrel (3), and BwEndCap (4) in the decay channel $h_c \to \eta_c\gamma \to \pi^0\pi^0\eta\gamma \to 7\gamma$. The results are presented for cluster threshold energies of 3 (white), 10 (dark gray), and 30 MeV (light gray). The percentages of the registered clusters after applying a cluster threshold of 10 MeV (upper numbers) and 30 MeV (lower numbers), as compared to the 3 MeV threshold, are also shown above the corresponding bars in the graph. The shaded regions in each bar correspond to the respective percentages for 1 GeV photons emitted isotropically from the target point. In this case, the presented results are determined for the equivalent number of decayed h_c resonances.

1 MeV, was found to be negligible. The beam energy was tuned to the production-threshold energy of 6623.1 MeV. This situation simulates the beam-scanning technique [1, 3] of resonances and a beam-energy width of 0.55 MeV was assumed corresponding to the high-luminosity case of the HESR ($\frac{\sigma_p}{p} \approx 10^{-4}$). For the decay width of the η_c, a value of 29.7 MeV was used taken from the PDG [18]. The angular distributions of the six decay gammas produced from the decay of η and the two π^0 resemble the one for the transition γ (dashed magenta line) in fig. 21(c). The decay probability is peaked around 25° and 6° for the decay angles of the transition γ and the η_c, respectively. Comparing fig. 21(a) and (b), it is also interesting to note that the most forward-scattered transition γ (η_c particles) are the most (least) energetic, as the total energy of the transition γ and η_c should remain conserved.

The lookup table defined in sect. 3.4 was applied for the analysis of the $h_c \to \eta_c + \gamma$ channel to correct the cluster energies retrieved with PandaROOT. Figure 22 shows the simulation results for the distribution of the four EMC modules registering clusters for the decay channel $h_c \to \eta_c\gamma \to \pi^0\pi^0\eta\gamma \to 7\gamma$. The results are presented for cluster threshold energies of 3, 10, and 30 MeV. The percentages of the registered clusters after introducing cluster threshold energies of 10 and 30 MeV, as compared to the 3 MeV threshold, are also presented in this figure for different modules. The additional bias on the average number of clusters when we introduce a 30 MeV rather than a 10 MeV threshold is about 5% for each EMC module except for the FwEndCap for which the average number of clusters shrinks by about 10%.

If we perform the same simulations with seven uncorrelated photons of 1 GeV emitted isotropically from the target point, we get about the same results (the corresponding percentages are indicated by the shaded bars in fig. 22). It should be noted that the FwEndCap exhibits a larger reduction in the detected number of clusters than the other modules for a 10 MeV cluster threshold relative to the 3 MeV threshold. This effect is related to the previously mentioned overlap of the forward edge of the Barrel EMC with the FwEndCap circumference.

4.2 Signal invariant-mass reconstruction

In order to reconstruct the invariant mass for pairs of registered clusters, one can make use of the following equation for the 2γ-decay of π^0 and η:

$$M_{\pi^0,\eta} = \sqrt{2E_1E_2(1-\cos\theta)}, \qquad (5)$$

where $M_{\pi^0,\eta}$ is the invariant mass of the supposed π^0 or η particles, while E_1, E_2, and θ represent the reconstructed energies and opening angle between the two clusters under

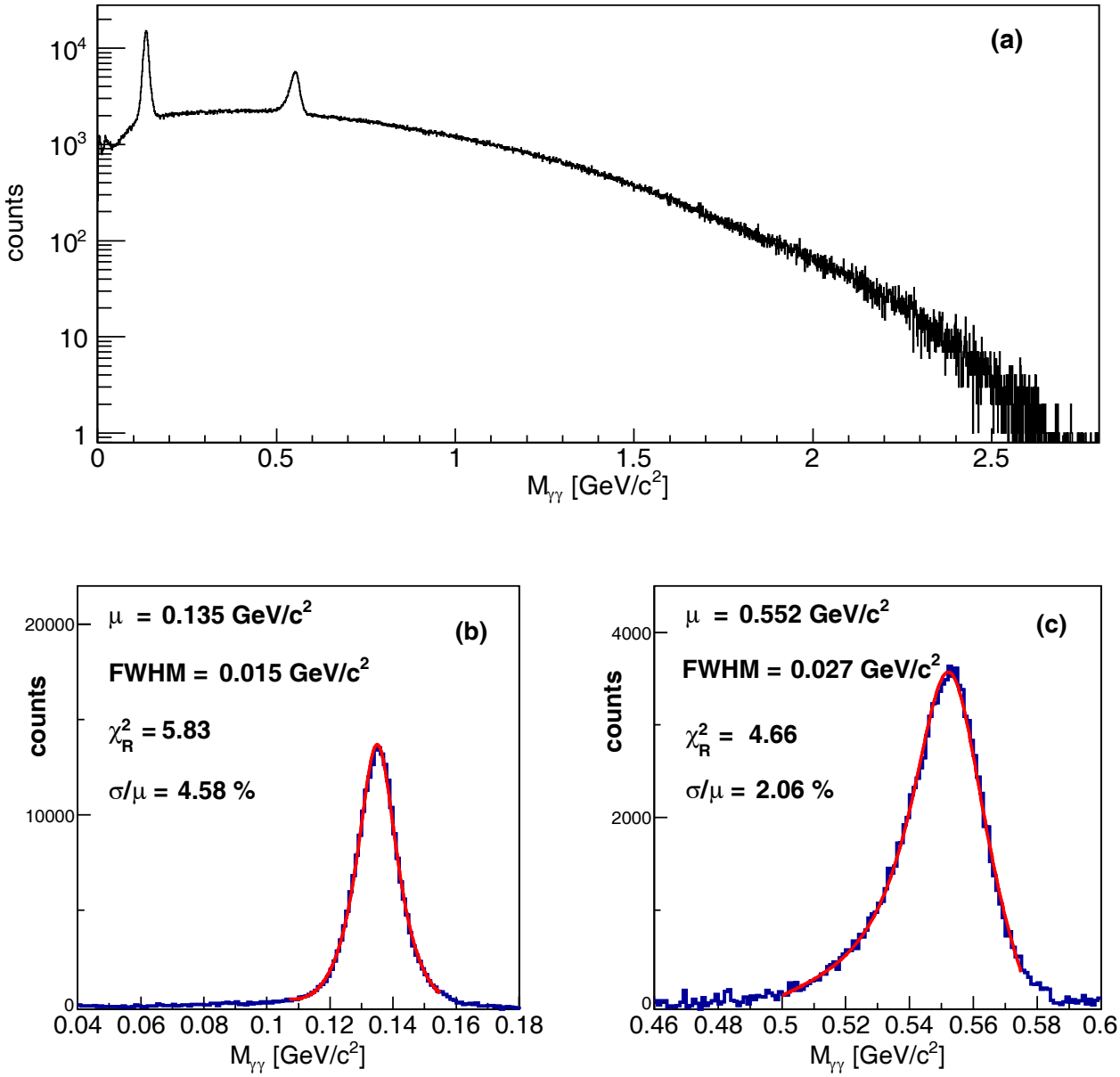

Fig. 23. The invariant-mass spectrum, reconstructed in the simulations of the full EMC, taking into account the contribution of all combinations of clusters that would possibly reproduce π^0 (b) and η (c) particles before (a) and after (b and c) background subtraction. A threshold energy of 30 MeV is considered for all the clusters reconstructed by various EMC modules and a 1.5%/cm non-uniformity is introduced only for the Barrel crystals. The fits are Lorentzian functions whose peak positions μ [GeV] and FWHM [GeV] are indicated in the lower panels.

analysis, respectively. In the simulations of the h_c decay to $\eta_c\gamma \to \pi^0\pi^0\eta\gamma \to 7\gamma$, we took all the possible combinations of choosing 2 photons out of the number of registered clusters satisfying the cluster threshold energy. The total number of cluster combinations is the binomial coefficient $\binom{N_{cl}}{2}$, in which N_{cl} is the number of registered clusters per event. Thus, the invariant mass histogram is filled $\binom{N_{cl}}{2}$ times per event for those events with $N_{cl} \geq 7$. In this analysis we observed a maximum of 17, 33, and 67 registered clusters in the EMC, when we introduced cluster threshold energies of 30, 10, and 3 MeV, respectively. Figure 23 shows the reconstructed invariant-mass spectra of π^0 and η particles before and after subtracting the combinatorial background extracted from polynomial fitting, requiring at least 7 clusters to satisfy a cluster threshold energy of 30 MeV.

The invariant-mass spectrum of π^0/η can be employed to reconstruct the invariant masses of η_c and h_c. In the case of η_c, the total number of cluster combinations per event is $\binom{N_{cl}}{6}$ for those events with $N_{cl} \geq 7$. For each cluster combination, the invariant mass is calculated as the magnitude of the total four-momentum of the 6 clusters

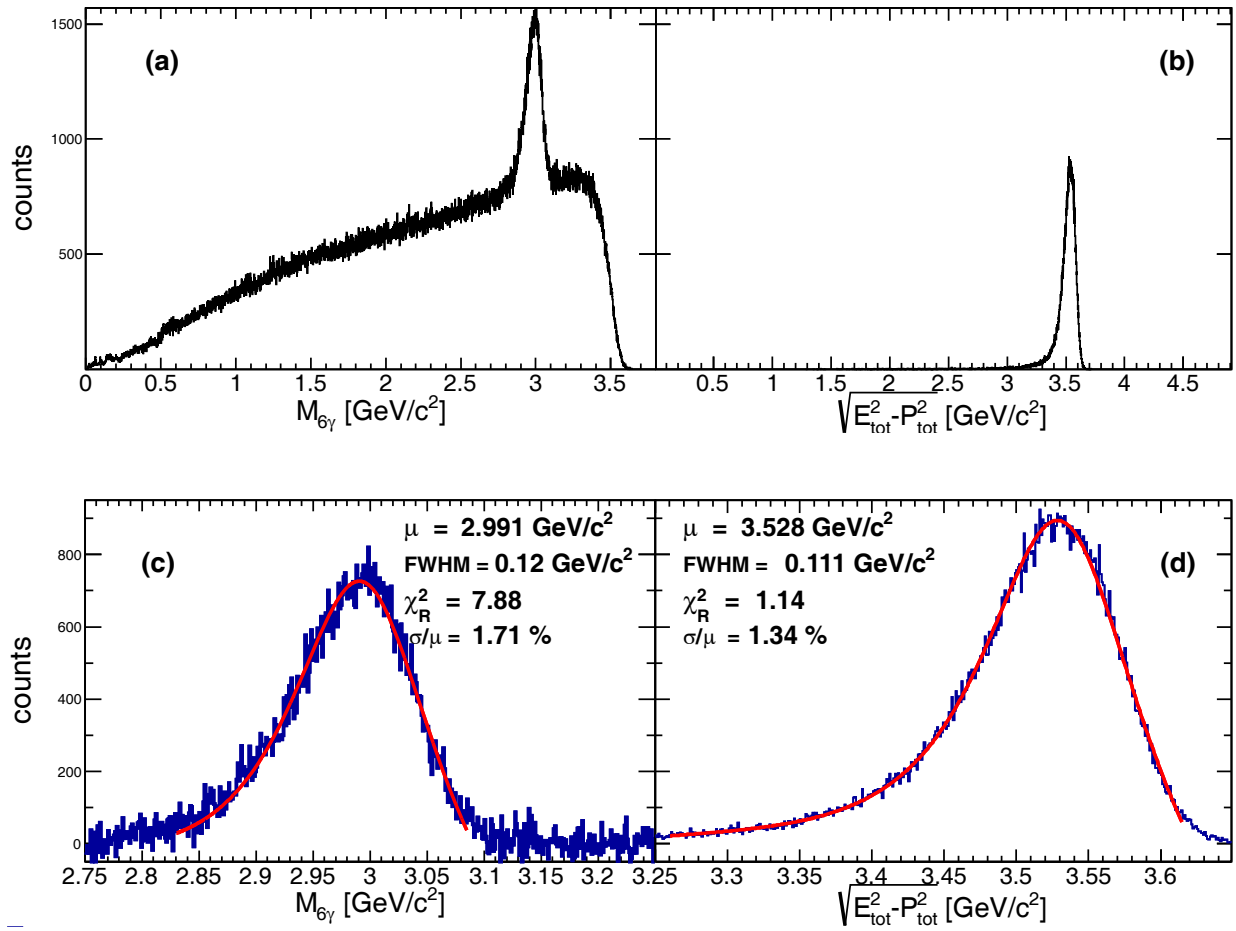

Fig. 24. Left panels: the invariant mass spectra of η_c, reconstructed in the simulations of the full EMC, taking into account the contribution of all combinations of clusters that would possibly reproduce η_c particles before (a) and after (c) background subtraction. The number of combinations per event for η_c is $\binom{N_{cl}}{6}$, with N_{cl} (≥ 7) being the number of clusters satisfying the cluster threshold energy of 30 MeV. In the case of h_c (right panels), no background (b), expanded view in (d) is assumed to be subtracted due to the way the h_c spectrum is reconstructed: the invariant mass is calculated as the magnitude of the total four-momentum of all registered clusters for events with $N_{cl} \geq 7$. The fits and parameters are defined as in fig. 23.

satisfying the cluster threshold. One can, in principle, follow the same procedure and add up the contribution of $\binom{N_{cl}}{7}$ combinations of clusters to get the invariant-mass spectrum of h_c. However, we did obtain this spectrum by taking the magnitude of the total four-momentum of all registered clusters with total number of $N_{cl} \geq 7$ per event. This way, we remove the huge amount of the combinatorial background that unavoidably enters in the cases of π^0, η, and η_c due to the wrong combinations of clusters. Figure 24 shows the reconstructed spectra of the invariant masses of the h_c and η_c (before and after background subtraction), assuming a 30 MeV cluster threshold.

Table 3 summarizes the fitting parameters for the spectra of the invariant masses and total energy of all clusters, together with the derived resolutions in detecting π^0, η, η_c, and h_c particles, assuming cluster threshold energies of 10 and 30 MeV. The resolutions are provided for the three cases of having the full EMC, or only the FwEndCap, or the full $\overline{\text{P}}$ANDA detector (including magnets, pipe, STT, MVD, MTD, GEM, DIRC, DSK, FTS, FTOF, SciTil) present in the analysis. It is interesting to note that, for π^0 and arguably for η, the resolution results derived from the FwEndCap are slightly better than the ones extracted from the full EMC analysis. This is due to the boost in the forward angles, where the two high-energy photons detected by the FwEndCap would ensure a relatively better resolution than when they would be detected at larger opening angles by different EMC modules. The mean values of the π^0 and η invariant masses reconstructed by the FwEndCap, as the only EMC module present in the geometry, are overestimated as compared with the ones obtained by the full EMC. This is due to the shower leakage from the corner edges of the FwEndCap and the performance of the lookup table for these regions. Clearly, this would not be the case for the full EMC geometry as, seen from the target point, the corner edges of the FwEndCap are covered by the Barrel forward edges.

Table 3. Fitting parameters for the spectra of the invariant masses and total cluster energies as well as derived resolutions (FWHM/2.35) in detecting π^0, η, η_c, and h_c particles in the h_c decay channel, assuming a cluster threshold energy of 30 (10) MeV. All spectra were obtained by taking into account the contribution of only those events with at least 7 clusters satisfying the threshold. The results are shown for the three cases of having the full EMC, or only the FwEndCap, or the full $\overline{\text{P}}$ANDA detector present in the analysis. Clearly, the geometrical acceptance of the FwEndCap does not allow detecting simultaneously the 6 or 7 gammas emitted from the decay of η_c or h_c. For the error calculation, the quality of fitting has been taken into account through multiplying the error boundaries by $\sqrt{\chi^2_R}$ to obtain the indicated error boundaries.

Decayed particle	μ [MeV]	FWHM/2.35 [MeV]	χ^2_R	resolution [%]
Full EMC				
π^0	134.98 ± 0.02	6.18 ± 0.05	5.83	4.58 ± 0.1
	(134.74 ± 0.02)	(6.11 ± 0.04)	(6.18)	(4.53 ± 0.07)
η	552.12 ± 0.07	11.38 ± 0.18	4.66	2.06 ± 0.06
	(552.3 ± 0.09)	(11.35 ± 0.25)	(6.92)	(2.05 ± 0.13)
η_c	2990.6 ± 0.4	51.01 ± 0.72	7.88	$1.71^{+0.06}_{-0.08}$
	(2993.1 ± 0.38)	(50.12 ± 0.83)	(7.64)	$(1.67^{+0.08}_{-0.05})$
h_c	3528.44 ± 0.36	47.42 ± 0.72	1.14	1.34 ± 0.02
	(3530.5 ± 0.38)	(46.54 ± 0.63)	(1.23)	(1.32 ± 0.02)
h_c	6650.78 ± 0.53	73.7 ± 1.05	1.04	$1.11^{+0.01}_{-0.02}$
total energy	(6661.08 ± 0.43)	(72.71 ± 0.89)	(1.35)	(1.09 ± 0.01)
FwEndCap				
π^0	137.68 ± 0.05	5.81 ± 0.12	3.76	4.22 ± 0.17
	(137.45 ± 0.06)	(5.59 ± 0.11)	(4.86)	$(4.07^{+0.18}_{-0.2})$
η	554.25 ± 0.36	10.12 ± 0.82	3.71	$1.82^{+0.29}_{-0.27}$
	(554.71 ± 0.46)	(10.88 ± 0.75)	(4.23)	(1.96 ± 0.29)
Full $\overline{\text{P}}$ANDA Detector				
π^0	134.76 ± 0.03	6.34 ± 0.06	5.6	$4.70^{+0.12}_{-0.09}$
η	551.97 ± 0.05	12.43 ± 0.14	4.2	$2.25^{+0.06}_{-0.04}$
η_c	2981.05 ± 0.41	53.06 ± 0.19	6.17	1.78 ± 0.02
h_c	3520.32 ± 0.56	48.23 ± 0.78	2.14	1.37 ± 0.03

5 Discussion of simulation results

Simulations were performed with photons emitted isotropically from the target as well as hitting specific crystals inside the FwEndCap. Subsequently, various analyses were performed including the full-energy efficiency and the energy and position resolutions. For 1 GeV isotropically-emitted photons, the position resolution of $\sigma_{x,y} \approx 3.3$ mm for cluster reconstruction was obtained, which can be compared with the front-face extension of the crystal (24.37 mm). An investigation of the energy-weighting parameters resulted in best position resolutions for the FwEndCap, once we introduced

$$W_0 = 4.071 - 0.678 \times \left(\frac{E_{cl}}{\text{GeV}}\right)^{-0.534} \cdot \exp\left(-\left(\frac{E_{cl}}{\text{GeV}}\right)^{1.171}\right).$$

The multiplicity distribution after digitization showed a significant sensitivity to the detection threshold of individual crystals. As a result of the partial overlap of the FwEndCap circumference with the forward edge of the Barrel EMC, a shift to a lower mean *digi* multiplicity is observed. This effect can be considerable for high photon energies at high detection thresholds. The cluster-multiplicity distribution reveals as well a drastic sensitiv-

Table 4. Parameters and design performance of the EMC in various experiments compared with the ones of the $\overline{\mathrm{P}}$ANDA EMC. The results for the $\overline{\mathrm{P}}$ANDA and BESIII [24] calorimeters are from the Monte Carlo simulations.

Parameter	$\overline{\mathrm{P}}$ANDA	BESIII	CLEO-c [25]	BaBar [17]	Belle [26]
Radiation length (X_0)	22	15	16	$16-17.5$	16.2
σ_E [MeV] at 1 GeV	25.4	≈ 25	≈ 20	≈ 28	≈ 17
σ_E [MeV] at 100 MeV	6.6	3.3	4	4.5	4
Position resolution (σ) [mm] at 1 GeV	3.3	6	4	4	6

ity to the cluster threshold as expected; for 1 GeV photons and assuming a 30 MeV (10 MeV) cluster threshold, one would expect 99.6% (97%) of events to have a maximum of two registered clusters. In principle, however, one has to be careful when implementing cluster thresholds in the analysis, *e.g.* when one needs to achieve π^0 background suppression based on the analysis of low-energy photons. Although we chose, in this paper, to suppress the split-off clusters by optimizing the cluster threshold, there is a need for more refined algorithms exploiting the threshold dependence. The investigation of the full-energy efficiency of the FwEndCap as the only module in the geometry showed that, for a 3 MeV *digi* threshold, one can expect a collection efficiency of about 95% for the photon energies ranging from 1 GeV to 10 GeV. The efficiency would decrease to 93% as the photon energy decreases from 1 GeV to 100 MeV. Although the efficiency shows considerable sensitivity to the detection threshold at low photon energies, it would only change slightly (0.5%) for high-energy photons.

A comparison of the energy resolutions from simulations and the PROTO60 experiment with a sensitivity of 52 photo-electrons/MeV and 2 MeV *digi* threshold shows very good agreement with less than 0.5% worse resolution (σ/μ) of PROTO60 at low energies of the order of 100 MeV. We verified that the energy resolution for the Barrel-type crystals, in the energy range from about 100 MeV to 1.4 GeV, satisfies the functional form $\sigma/\mu[\%] = 1.95 \oplus \frac{1.9}{\sqrt{E/\mathrm{GeV}}}$ which is close to the requirement stated in [3], *i.e.* $\sigma/E[\%] \leq 1 \oplus \frac{\leq 2}{\sqrt{E/\mathrm{GeV}}}$.

For isotropic photon emission from the target and by increasing the cluster threshold from 3 MeV to 10 MeV, the number of clusters in each of the four modules of the EMC would diminish by about 50%. The reason for a slightly stronger reduction of clusters in the FwEndCap lies in the partial overlap with and screening by the Barrel EMC.

The simulation studies for the FwEndCap EMC were completed by analysing a representative physics channel. The charmonium h_c decay into $\eta_c\gamma$, assuming a decay probability proportional to $\sin^2(\theta_{CM})$, and the subsequent decay into $\pi^0\pi^0\eta\gamma$ were implemented in the event generator with π^0 and η decaying into 2 photons. The analysis of this channel was conducted for the two cases of having the FwEndCap as the only EMC module in the analysis as well as for the full EMC. The constructed lookup table for energy-direction corrections of the clusters as a function of their energy and polar angle allowed to reconstruct invariant-mass peak positions and resolutions of the h_c and its various decay products π^0, η, and η_c.

The parameters and expected performance of the $\overline{\mathrm{P}}$ANDA EMC, based on prototype data and Monte Carlo simulations, can be compared with the corresponding ones of other (running) experiments, as presented in table 4. The EMC calorimeters in CLEO-c, BaBar, Belle, and BESIII detectors were all made of CsI(Tl) crystals. The design energy resolution of EM showers in BESIII is about 2.5% and 3.3% for photon energies of 1 GeV and 100 MeV, respectively. The corresponding resolutions for the Barrel EMC of $\overline{\mathrm{P}}$ANDA in the presence (absence) of non-uniformity were obtained to be 2.5%$\widehat{=}$25.4 MeV (1.3%$\widehat{=}$12.7 MeV) and 6.6%$\widehat{=}$6.6 MeV (5.5%$\widehat{=}$5.6 MeV), respectively. The Monte Carlo result for the mass resolution of the π^0 reconstructed by the BESIII EMC in the decay channel of $J/\psi \to \rho\pi$ with $\pi^0 \to \gamma\gamma$ has been determined to be $\sigma_M = 7.3$ MeV [24]. We obtained a slightly better mass resolution of $\sigma_M = 6.2$ MeV for the π^0 in the decay channel of h_c to $\pi^0\pi^0\eta\gamma$ using the $\overline{\mathrm{P}}$ANDA EMC.

6 Conclusions

The mechanical design of the Forward End-cap EMC is ready for construction. Based on the defined geometry, the $PbWO_4$ crystals and the carbon-fiber containers (alveoles) were implemented in the PandaROOT simulation package. Simulations have been validated by prototype experiments. The obtained energy resolutions of the Barrel-type crystals are satisfactory and close to the expectations raised by the technical design report. The overlap between the Barrel and the Forward End-cap EMC causes modifications of the observed cluster distributions. The optimized analysis of this overlap region requires developing a dedicated reconstruction algorithm. The analysis presented here shows that the overlap effects are of minor importance for the overall performance of the electromagnetic calorimeter.

The authors thank Prof. N. Kalantar-Nayestanaki for useful comments. The authors also thank the EMC and computing groups of the $\overline{\mathrm{P}}$ANDA Collaboration for their useful comments and suggestions. This work was supported by the GSI Helmholtzzentrum für Schwerionenforschung GmbH, Germany, the University of Groningen, and the Dutch Organization for Scientific Research (NWO).

References

1. The $\overline{\mathrm{P}}$ANDA Collaboration (W. Erni *et al.*), *Physics Performance Report for $\overline{\mathrm{P}}$ANDA: Strong Interaction Studies with Antiprotons*, arXiv:0903.3905v1 [hep-ex] (2009).
2. A. Lehrach *et al.*, Nucl. Instrum. Methods A **561**, 289 (2006).
3. The $\overline{\mathrm{P}}$ANDA Collaboration (W. Erni *et al.*), *Technical Design Report for $\overline{\mathrm{P}}$ANDA Electromagnetic Calorimeter (EMC)*, arXiv:0810.1216v1 [physics.ins-det] (2008).
4. R. Novotny *et al.*, IEEE Trans. Nucl. Sci. **47**, 1499 (2000).
5. The CMS Collaboration, *CMS Technical Proposal*, CERN-LHCC-94-38, LHCC-P-1 (1994) `http://cds.cern.ch/record/290969/files/cer-0212026.htm`.
6. M. Kavatsyuk *et al.*, Nucl. Instrum. Methods Phys. Res. A **648**, 77 (2011).
7. The CMS Collaboration, *CMS Physics Technical Design Report*, CERN/LHCC (2006).
8. S. Spataro *et al.*, J. Phys.: Conf. Ser. **331**, 032031 (2011).
9. R. Brun, F. Rademakers, Nucl. Instrum. Methods Phys. Res. A **389**, 81 (1997).
10. `http://root.cern.ch/root/vmc`.
11. S. Agostinelli *et al.*, Nucl. Instrum. Methods Phys. Res. A **506**, 250 (2003).
12. `http://www.kve.nl`.
13. Unigraphics UGS NX7.5 CAD/CAM/CAE design software package.
14. D.J. Lange, Nucl. Instrum. Methods Phys. Res. A **462**, 152 (2001).
15. M. Burchell, Hadronic split-offs, CB Note 201 (1992) `http://argus.phys.uregina.ca/gluex/DocDB/0014/001448/001/CBAR_Hadronic_Splitoffs.pdf`.
16. T.C. Awes *et al.*, Nucl. Instrum. Methods Phys. Res. A **311**, 130 (1992).
17. B. Aubert *et al.*, Nucl. Instrum. Methods Phys. Res. A **479**, 1 (2002).
18. Particle Data Group (J. Beringer *et al.*), Phys. Rev. D **86**, 010001 (2012) `http://pdg.lbl.gov/`.
19. S. Grape, Licenciate Thesis, Uppsala University (2008) arXiv:0805.0950.
20. H. Löhner *et al.*, IEEE Trans. Nucl. Sci. **59**, 2237 (2012).
21. D. Bremer *et al.*, Poster presented at the 12th International Conference on Inorganic Scintillators and their Applications, SCINT 2013, April 15–19, 2013, Shanghai, China and D. Bremer, PhD thesis, University of Giessen, Germany (2013) in publication.
22. M. Ablikim *et al.*, Phys. Rev. D **86**, 092009 (2012).
23. M.G. Olsson, Casimir J. Suchyta, III, Phys. Rev. D **34**, 2043 (1986).
24. M. Ablikim *et al.*, Nucl. Instrum. Methods A **614**, 345 (2010).
25. Y. Kubota *et al.*, Nucl. Instrum. Methods Phys. Res. A **320**, 66 (1992).
26. A. Abashian *et al.*, Nucl. Instrum. Methods Phys. Res. A **479**, 117 (2002).